

Performance Analysis of Zero-Padded Sequences for Joint Communications and Sensing

Sayed Hossein Dokhanchi , André Noll Barreto , *Senior Member, IEEE*, and Gerhard P. Fettweis , *Fellow, IEEE*

Abstract—Self-interference (SI) is a known but critical issue at the receiver side of a monostatic radar in joint communications and sensing (JCAS) systems, and this is particularly true for high spectral-efficient waveforms. Full-duplex transceivers are usually assumed in the literature, but it is arguable if they can be taken for granted in many devices. We propose a different approach, by eliminating the SI using zero-padded (ZP) orthogonal frequency-division multiplexing (OFDM) and single-carrier frequency-division multiple access (SC-FDMA), instead of the more widespread cyclic-prefix (CP)-OFDM. ZP-sequences do not need full-duplex for the monostatic radar operation, as there is no SI between the transmit and receive antennas during the guard interval (GI), which can be used for radar detection. We derive the required radar receiver processing for ZP-sequences and CP-OFDM in time and frequency domains, respectively, to show that when the SI in JCAS is high, ZP-sequences can be beneficial, depending on the target range. Furthermore, we prove analytically that the low peak-to-average power ratio (PAPR) of ZP-SC-FDMA, when compared to ZP-OFDM, is beneficial in time-domain radar processing. This is demonstrated also by means of numerical simulation with ROC curves, for all the candidate waveforms in both coherent and incoherent receiver processing.

Index Terms—Joint communications and sensing, Self-interference, Monostatic radar, Coherent and incoherent processing, Full-duplex transceivers, Zero-padded (ZP) orthogonal frequency-division multiplexing (OFDM), Single-carrier frequency-division multiple access (SC-FDMA), Cyclic-prefix (CP)-OFDM.

I. INTRODUCTION

JOINT communications and sensing (JCAS) is likely to be one of the key features in 6G wireless networks [1], promising a more efficient use of hardware and spectrum. Besides, it will allow the creation of a plethora of new applications that can profit from the new offering of radar as-a-service (RaaS). Integrated communications will also improve the radar performance, since this will enable sensor fusion using connected distributed radars [2], as well as facilitate interference management by means of better coordination [3]. The communications networks will also profit from sensing data, for instance by using this information to improve beam allocation [4]. Intensive research efforts have been devoted for developing this technology in the

last decade, witnessing a booming interest from both academia and industry on the joint system, due to its significant potentials in emerging networks.

Most of the research work in this topic is concentrated on the study of different waveforms seeking to merge the communication and sensing functionalities into a joint shared platform with common waveform and hardware [5], [6], [7]. This framework is usually called co-design in the literature [8]. Such an approach is beneficial for both systems by relaxing the spectrum congestion and offering an efficient alternative scheme compared to two stand-alone systems. In this regards, a novel simple radar receiver processing has been proposed for a bistatic JCAS in a vehicular scenario using conventional waveforms such as orthogonal frequency-division multiplexing (OFDM) and phase modulated continuous waveform (PMCW) [9]. It has been proved analytically that in a *bistatic* JCAS, the parameter identifiability does not hold when communications signal is integrated into the radar waveform, due to the rank-deficiency of the Fisher-information matrix. Thus a bistatic JCAS requires an efficient multiplexing strategy to deal with identifiability problems. In this work, the JCAS has no access to prior information about the environment. The other line of research is to benefit from this prior knowledge being available to the JCAS from previous radar scans. Given this information, an optimum waveform can be designed to maximize the signal-to-clutter-plus-noise ratio (SCNR) at the radar receiver side while maintaining a good communications performance at the communications side [10]. A full-duplex IEEE 802.11 ad-based radar has been proposed that exploits the preamble of a single-carrier physical layer frame to simultaneously achieve range estimation and Gbps data rates [11]. To improve this further, [12] has been proposed a system that transmits non-uniformly placed preambles for enhancing velocity estimation accuracy, at the cost of a reduction in the communication data rate. It shows that optimal non-uniform preambles achieve a significant performance improvement as compared to a uniform waveform [12]. However, we discuss later that having a full-duplex JCAS such as [11], [12] has many hardware difficulties and will develop our solution to deal with this challenge. The frequency-modulated continuous wave (FMCW) signals, which are currently extensively used in radar systems, have also been proposed for JCAS application [13]. FMCW allows the implementation of relatively simple transceivers, but, does not offer high spectral efficiency as OFDM. FMCW-JCAS imposes less complexity for self-interference (SI) suppression compared to cyclic prefix (CP)-OFDM, since SI can be cancelled through down-mixing with the modulated transmit waveform [14].

Many literature on waveform design for JCAS consider the use of OFDM [15], [16], [17]. A radar image can be created from a CP-OFDM signal, either through correlation-based

Manuscript received 21 September 2022; revised 9 March 2023; accepted 20 April 2023. Date of publication 8 May 2023; date of current version 19 May 2023. The associate editor coordinating the review of this manuscript and approving it for publication was Prof. Ya-Feng Liu. (*Corresponding author: Sayed Hossein Dokhanchi.*)

The authors are with the Barkhausen Institut, 01187 Dresden, Germany (e-mail: hossein.dokhanchi@barkhauseninstitut.org; andre.nollbarreto@barkhauseninstitut.org; gerhard.fettweis@barkhauseninstitut.org).

Digital Object Identifier 10.1109/TSP.2023.3273331

processing or modulation symbol-based processing. In correlation processing, the two issues are the repetition of samples as CP which is the most dominant degrading factor as well as the high peak-to-average power ratio (PAPR) of CP-OFDM. However with the alternative approach called modulation symbol-based processing in which after removing the CP in time-domain, the symbol-based demodulation has been performed in frequency-domain and then the rest of the signal at frequency-domain has been used for radar. This method outperforms radar performance in comparison with correlation-based processing due to avoiding the two aforementioned problems [15]. In our paper, we employ the latter to deal with the high PAPR and CP regarding CP-OFDM. However, the problem of SI is still left there. Some literature on waveform design for JCAS consider the use of extensions of the multicarrier concept, like orthogonal chirp-division multiplexing (OCDM) [18] or orthogonal time frequency space (OTFS) [19]. Nevertheless, when compared with FMCW, multicarrier modulation schemes have some disadvantages in terms of hardware complexity, such as the high PAPR, the requirement of analog-to-digital converters (ADCs) with high sampling rate and high resolution, and the need for in-band full-duplex (FD). It is well known that the radar echoes are usually received with a very low power, as the received power decays with the fourth power of the range, and the SI can be many orders of magnitude stronger than the desired echo. The SI can thus saturate the low-noise amplifier (LNA) hampering the echo detection, and the receiver needs a programmable gain amplifier or an automatic gain controller to manage that combined with additional active power consuming circuitry to mitigate the adverse impact on ADC. There have been recently lots of research activities on FD, but real-life implementations are, however, costly and energy hungry, besides providing just limited isolation between transmit (TX) and receive (RX) [20]. Whereas the literature has shown that FD is possible, it is not expected to be available in most devices in the near future.

Various methods for SI cancellation have been studied in the literature with emphasis on improved TX-RX isolation level. However, most of the solutions require a combination of analog and digital filters which are nonlinear, power hungry and costly to suppress the SI. It has been confirmed that from the CP-OFDM radar processing perspective, limited SI is primarily a concern in the detection of static targets [14]. Thus, one solution is to filter out the stationary targets including the SI from the transmitter, where SI mimics a stationary target with approximately zero range and large radar cross section (RCS) [21]. The drawback is that this type of SI cancellation is just applicable for detection of the moving targets. In another work, two separate radar sensing functions have been designed for short-range and long-range sensing [22] to suppress SI. Thus, the correlation properties of Golay sequences in the preamble have been leveraged for short-range radar sensing. Though there is no need for SI channel estimation, calculating the cross-correlation of the Golay code in the existence of strong SI is still erratic. Another approach is to map the problem in frequency domain and solve it with null-space projection (NSP). In NSP, the SI channel between TX streams and the sensing RX chains is first estimated and then canceled through corresponding RX beamformer matrix [23]. In particular, the SI is projected into the null-space spanned by the columns of RX beamformer matrix. However, the multi-antenna SI channel is usually not known and the impact of imperfect SI channel estimation on the performance may become very significant. Another technique is to combine SI cancellation

approaches such as physical, analog, and digital mitigation techniques for JCAS [24]. A combination has been demonstrated to suppress SI in the order of 100 dB, for a FMCW-JCAS system [24]. Active analog cancellation uses adaptive multi-tap filters to mimic the channel and the transmit signal as the reference to generate the cancellation signal. However, the problem with FMCW is that it has a low spectral efficiency for communications which yields a low data rate, and also the range-Doppler coupling problem in radar processing can limit the performance [25]. Analog domain SI cancellation is a promising technique because passive methods are typically employed in this domain, while digital suppression is limited by the precision of the ADC [24]. To mitigate the SI issue, an analog cancellation circuit can be utilized to cancel a portion of the SI. The signal that follows analog SI cancellation is then directed to the digital signal-processing modules of either the communication or radar system. However, despite these measures, the resulting radar signal-to-self-interference ratio (RSSIR) is still relatively low and requires further improvement.

Many SI suppression schemes are not robust when the SI is complex and non-linear such as in our case with CP-OFDM. Deep learning (DL) techniques are being explored for the SI suppression, because they can learn complex non-linear decision boundaries [26]. The key benefit of using DL is the ability to learn non-linear relationships for interference suppression which would be difficult to develop through traditional suppression techniques [26]. However, requiring a large repository of dataset, making DL-SI suppression a very challenging task, since generating enough data for different realizations of all possible transmit signals is very time-consuming.

In our proposed method, we have employed random data payloads for sensing. It is apparent that the radar component of the JCAS terminal, which serves also as the transmitter of the communication system, is aware of this random data. The detection probability can be affected by the randomness of the data, which can result in suboptimal radar characteristics. The characteristics of a suitable radar waveform can typically be determined by analyzing its ambiguity function (AF). However, the impact of the randomness can be reduced by increasing the sequence length. It is worth noting that while the dependency of the waveform on random data payload may not be ideal for detection purposes, it does offer a level of security. This is because the noise-like sequence is difficult for unauthorized parties to detect.

Here, we propose a new approach, in which instead of the widespread CP, we use zero-padded (ZP) suffixes. By doing that, we can use the guard intervals to detect radar reflections by switching the modem from transmit to receive, with no need for FD, as there is no SI during the guard interval (GI), which can be used for radar detection. In fact, we are actually making the monostatic radar a half-duplex (HD) system, simplifying hardware design. The PAPR issue can be solved, as widely known, by employing single-carrier orthogonal frequency-division multiple access (SC-FDMA), also with ZP, which, as we will see, is also beneficial for radar detection. Communications with ZP-OFDM have already been addressed in the literature with some simple solutions such as overlap-and-add (OLA) method [27].

Our proposed method can be applied to both stationary and moving targets, unlike [21]. Differently from [23] it also does not require estimates of the SI channel at all and can also be applied to single antennas. The concept of employing ZP-OFDM for JCAS was introduced in our previous work [28]. It has

been shown there that when the SI in CP-OFDM is high when compared with the reflected echo, then ZP-OFDM is beneficial. This is particularly the case for farther targets. However, this study surpasses [28], and has several significant distinctions as follow:

- One of the novel contributions of this study, in contrast to [28], is demonstrating that a high PAPR results in poor radar performance for ZP-sequences.
- The previously proposed ZP-OFDM system in [28] was found to have high PAPR, which negatively impacts radar performance. This study proposes a solution to mitigate the issue of high PAPR to improve radar performance.
- In [28], we only presented simulation results without any analytical explanation of the radar performance. This study provides a detailed analysis of the performance of different methods by deriving false alarm and detection probability analytically.
- Unlike our previous work, this study includes the derivation results for both *coherent* and *incoherent* processing.

Notation: Throughout this paper, bold lowercase and bold uppercase denote vectors and matrices, respectively. The transpose, Hermitian (conjugate transpose), Moore-Penrose pseudo-inverse, and inverse are designated by $(\cdot)^T$, $(\cdot)^H$, $(\cdot)^\dagger$ and $(\cdot)^{-1}$, respectively. The symbols \mathbb{C}^N and \mathbb{R}^N represent the set of N -dimensional vector of complex and real numbers, respectively. The $[a_{l,n}]_{l=0, n=0}^{L-1, N-1}$ represents a $L \times N$ dimension matrix with the entry $a_{l,n}$ at its l -th and n -th row and column, respectively. Similarly, $[a[l]]_{l=0}^{L-1}$ represents a L dimensional vector with the entry $a[l]$ at its l -th row. We also may write a vector with dimension N as $\mathbf{a} = [\mathbf{a}[0], \dots, \mathbf{a}[N-1]]^T$. The notation $\mathbf{A}[:, n]$ and $\mathbf{A}[n, :]$ denote the n -th column and the n -th row of \mathbf{A} , respectively. The matrix $\mathbf{0}_{L \times N}$ denotes a $L \times N$ matrix with all-zero elements. \mathbf{I}_N is the identity matrix of size N . \mathbf{e}_i represents the standard basis vector with a 1 in the i -th entry and all-zero elsewhere. The \mathbf{a}^{-1} means the element-wise inversion of the vector \mathbf{a} . The symbol \odot represents the Hadamard element-wise product. $\text{Re}\{\cdot\}$ and $\text{Im}\{\cdot\}$ give the real and imaginary part of the complex number, respectively. $\mathbb{E}(\cdot)$ takes the expectation of a random variable. The function $\text{diag}(\mathbf{a})$ outputs a diagonal matrix formed by the entries of vector \mathbf{a} , $\|\mathbf{a}\|$ denotes the Euclidean norm, i.e., the square root of the sum of the squares of the elements. The notation $a \sim \mathcal{CN}(\eta, \sigma^2)$ with complex number a means that a is a complex normal random variable with mean η and variance σ^2 . $a \sim \mathcal{N}(\eta, \sigma^2)$ with real number a means that a is a real normal random variable with mean η and variance σ^2 . $\text{Toep}(\mathbf{a}, :)$ denotes a Toeplitz matrix having vector \mathbf{a} on its first column, and $\text{Toep}(:, \mathbf{a}^T)$ denotes a Toeplitz matrix having \mathbf{a}^T on its first row. $\text{Circ}(\mathbf{a}^T)$ denote a circulant matrix where each column is a cyclic shift of the previous column, with \mathbf{a}^T as its first column. The function $Q_N(a, b)$ represents the generalized Marcum Q-function of order N , and $\mathcal{Q}(\cdot)$ is the right tail distribution function of the standard normal distribution. Throughout the paper, the symbols χ_ν^2 and $\chi_\nu'^2(\xi)$ stand for chi-squared probability density function (pdf) of degree ν and non-central-chi-squared pdf of degree ν with non-centrality parameter ξ , respectively. $\mathcal{I}_\alpha(\cdot)$ denotes the modified Bessel functions with index α .

Organization: The rest of the paper is organized as follows. Section II describes the scenario and discusses the challenges for CP-OFDM with in-band FD. The range processing for CP-OFDM at frequency domain is also presented. Section III discusses our proposed use of zero-padded communication

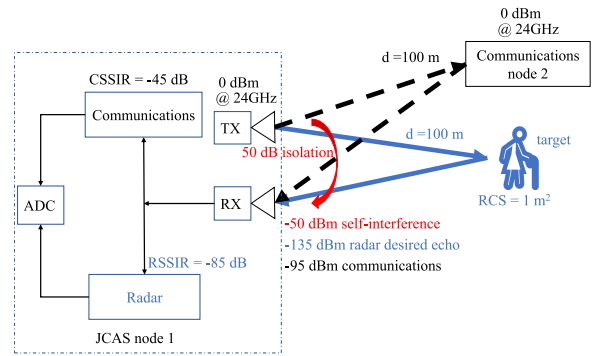


Fig. 1. scenario and challenge.

waveforms for sensing. We elaborate OFDM and SC-FDMA with zero-padding to clarify the range processing in time domain. Section IV is on the performance of the proposed detectors in closed-form solutions. We proposed five theorems which discusses the details of the receiver operating characteristics (ROC) curves for all waveforms under study. Section V contains all the simulation results, which confirm the closed-form formula of Section IV, and finally Section VI concludes the paper.

II. SIGNAL AND SYSTEM MODEL

A. Scenario and Motivation of the Work

Fig. 1 illustrates the system model and the challenges at full-duplex mode of JCAS. Note that here the radar receives the signal during the transmission time, i.e., it is full-duplex. With an ideal radio frequency (RF) front-end, the interference signal between transmitter and receiver will be manifested by a strong component in the first bins, which can in principle be discarded. In real receivers, however, the SI may saturate the LNA and the ADC, unless additional protection mechanism is followed yielding power overheads. This is more critical in radar receivers, i.e., $\text{RSSIR} = -85$ dB than in communication FD modems, i.e., communication signal-to-self-interference ratio ($\text{CSSIR} = -45$ dB, since the target echoes are usually strongly attenuated, with the fourth power of the range, (see Fig. 1).

The received power from the target echo can be calculated using the radar equation. This equation is expressed as follows:

$$P_r = \frac{P_t G_t G_r c^2 \sigma}{(4\pi)^3 f_c^2 d^4}, \quad (1)$$

where P_t is the transmit power, G_t and G_r are the gains of the transmitting and receiving antennas, respectively, c is the speed of light, σ is the RCS of the target, f_c is the carrier frequency, and d is the range to the target.

As an example, if we assume that P_t is known and equal to a certain value, and we have $G_t = G_r = 5$ dB, $\sigma = 1$ m², $f_c = 24$ GHz, and $d = 100$ m, then we can use (1) to calculate the received power P_r . In this case, the received power is approximately $P_t - 135$ dBm. Assuming a 50 dB TX-RX isolation and no supplementary SI suppression technique, the RSSIR is -85 dB. With this extreme level of interference, no target detection is possible. Despite implementing interference suppression, the signal power level at 24 GHz is still quite low due to path-loss, necessitating a strong LNA to amplify the power and pulse integration for radar detection. This poses a significant challenge, especially in urban areas where regulatory safety limits restrict the maximum allowable transmit power.

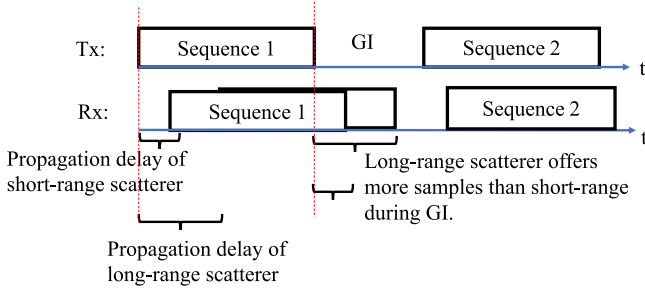


Fig. 2. the diagram illustrates the echoes from two targets with long and short ranges. There is more energy received by the echo of a long range target.

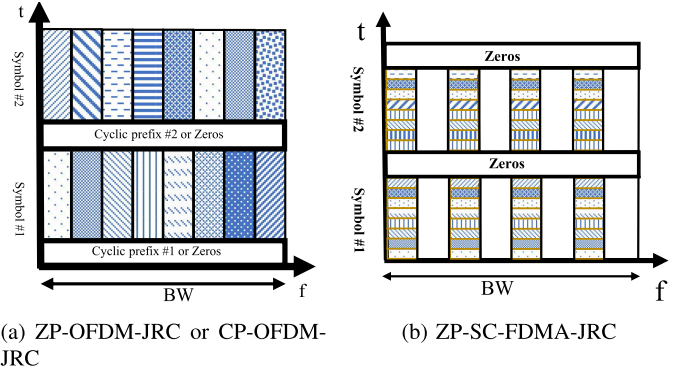
Also note that the isolation levels in the example may be optimistic, and higher isolation usually means higher costs. For example, we have assumed two separate antennas for TX and RX. With a single antenna, the isolation level would be even less. To address this issue, we propose employing zero-padded waveforms, which will be explained in greater detail in the subsequent section.

Unlike the existing schemes that apply complicated linear and non-linear analog and digital cancellation schemes before radar signal processing, the goal of this paper is to develop a radar sensing scheme that avoids the strong SI in the digital domain, by processing only the part of the signal that does not suffer any SI, i.e., the ZP guard interval. Thus, the computing complexity and power consumption for fully digital SI cancellation is removed, and lower-resolution ADCs can be employed.

The proposed method is depicted in Fig. 2, which demonstrates a portion of the echoes captured in the GI at the radar receiver. The signal received during the GI period is not subject to SI since the transmitter is not transmitting at that time. CP-OFDM suffers from SI in case of low isolation, although it benefits from the entire OFDM symbol for range recovery.

Note that the aim here is to compare the different methods such as ZP-sequences and CP-OFDM, and not how the same system performs in short and long ranges. Thus, in a fair comparison between short and long ranges, the effect of the propagation loss due to different distances should be neutralized. Consequently, we investigate both cases, i.e., far and near targets, under the *same received SNR*, which means more transmit power for the long ranges. Thus, we will see that our proposed ZP-sequence methods exhibit better performance for long-range targets than for short-range ones. The rationale is depicted in Fig. 2, which shows that the receiver is capable of capturing more energy from echoes in GI at longer ranges, even though the received power and the resulting signal-to-noise ratio (SNR) are the same. Specifically, the GI duration limits the amount of received power that can be captured, which is proportional to the propagation delay time. Consequently, shorter distances suffer from a greater performance degradation than longer distances because the fraction of received power that can be captured during the guard interval is smaller. Furthermore, to ensure an impartial comparison between two scenarios, it is necessary to maintain equivalent range bin sizes for both. This assumption is reasonable as the range resolution is equivalent across both scenarios.

Time-frequency spectrum: The time-frequency spectrum of all the waveforms being examined is displayed in Fig. 3. In Fig. 3(a), there are two symbols depicted, each consisting of 8 subcarriers in frequency-domain that can be distinguished by a



(a) ZP-OFDM-JRC or CP-OFDM-JRC

(b) ZP-SC-FDMA-JRC

Fig. 3. The diagram shows time-frequency spectrum of all the studied waveform.

distinct pattern in the figure. Either a sequence of zeros or a CP is inserted at the beginning of each symbol, depending on whether the waveform being used is ZP-OFDM or CP-OFDM.

In Fig. 3(b), the time-frequency spectrum of SC-FDMA is depicted, where in this example, the entire bandwidth is partitioned into four sections to implement the frequency division multiple access scheme, with two subcarriers in each band for two users. We select a single carrier from each frequency-band that the first user can utilize, and the remaining unoccupied carriers within each band, which are shown by white intervals, can be assigned to the second user. In Fig. 3(b), eight distinct patterns can be used to identify pulses in the time domain. Unlike OFDM, where each pulse carries multiple subcarriers, this system only uses four active subcarriers to transmit data and the rest of them are null subcarriers for the first user. Consequently, those null subcarriers that are present in each frequency band result in a lower PAPR compared to the waveforms illustrated in Fig. 3(a).

Use case scenario: Before we present the use case scenario, it is important to discuss about the impact of capturing the echoes in zero-padded time on the maximum unambiguous range (MUR). For ZP-sequences, it is obvious that we cannot make use of the full reflected wave, but only of its part that falls within the GI. This might also cause degradation of the MUR depending on the ratio of ZP time compared to the half of symbol-time, which can be presented by

$$t_{zp} > t_{sym}/2, \quad (2)$$

and in terms of distance

$$R_{MUR}^{CP} = \frac{ct_{sym}}{2}, \quad (3)$$

where c is the light velocity, $t_{zp} = t_{cp}$ is the cyclic prefix/ zero-padded time and t_{sym} is OFDM symbol-time. On the other hand, the most common choice for the length of the CP is a quarter of the length of the FFT used in the OFDM symbol, i.e., $t_{zp} \approx t_{sym}/4$. This is in a clear contrast with (2). Thus, we should trade the performance of communications and radar here. In order to avoid restriction on the communications performance, we set the $t_{zp} \approx t_{sym}/4$, and the MUR in this case is given by

$$R_{MUR}^{ZP} = \frac{ct_{zp}}{2} \approx \frac{ct_{sym}}{8}. \quad (4)$$

Thus we have

$$R_{MUR}^{ZP} \approx \frac{R_{MUR}^{CP}}{4}. \quad (5)$$

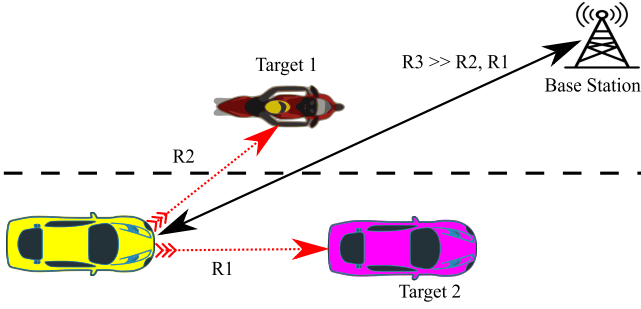


Fig. 4. A scenario where the yellow car is able to communicate with the base-station at a much greater distance of R_3 compared to detecting the bike at a distance of R_2 and the purple car in its nearby proximity at a distance of R_1 . As the base-station is located far away, the zero-padded interval is also sufficiently large to capture the echoes of target 1 and 2.

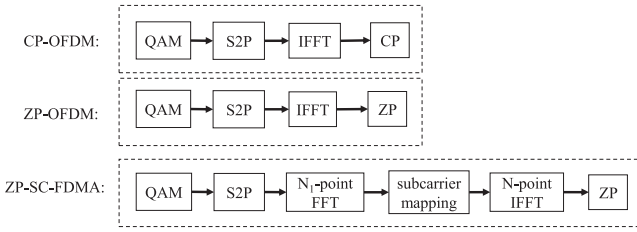


Fig. 5. transmit signal block diagram; S2P means serial to parallel function, CP is cyclic prefix insertion and ZP is zero padding operation.

Given the above equation, for a typical 5G-NR (New Radio) OFDM symbol-time of $t_{\text{sym}} = 8.33 \mu\text{s}$, we have

$$R_{\text{MUR}}^{\text{ZP}} \approx \frac{ct_{\text{sym}}}{8} = 312 \text{ m.} \quad (6)$$

One possible use case is in vehicular communications where a vehicle communicates with the base station usually locating at further distances e.g., 1 km away while illuminating its local vicinity with ZP-sequences up to 300 m. This scenario is depicted in Fig. 4. Furthermore, in this paper, we focus on the radar sensing only, since the communications performance of ZP waveforms has been extensively investigated in the literature [27], [29]. Furthermore, the radar sensing is focused only on the target detection and range estimation. This paper does not cover the process of Doppler and angle estimation for radar or the demodulation of communication symbols, as these tasks are considered straightforward.

B. Signal and System Model for CP-OFDM-JCAS

In this subsection, we describe the signal and the system model for CP-OFDM in FD mode as a monostatic radar inspired by [15]. Fig. 5 shows the block diagram of the transmit signal including all candidate waveforms. At each OFDM symbol the transmitter generates a sequence of N complex symbols representing the data, typically from a phase shift keying (PSK) or quadrature amplitude modulation (QAM) constellation. Let this sequence be denoted by $s[k]$, $0 \leq k \leq N - 1$, representing the complex amplitudes of each subcarrier. After taking an inverse fast Fourier transform (IFFT) at the transmitter, the signal in the time domain is represented by $x[l]$, $0 \leq l \leq N - 1$. The signal $x[l]$, or its equivalent in the frequency domain $s[k]$, is known at the radar receiver side, and can thus be used as reference to estimate the echoes from the received signal $y[l]$.

Radar detection with OFDM can be performed akin to round trip channel estimation with a known transmit signal in communications, as the channel impulse response will give us information about the reflections and their delays. We name the round trip impulse response which corresponds to the radar processing as environment impulse response (EIR) matrix.

We know that $x[l]$ has a high amplitude variations in time domain, as it is the sum of multiple subcarriers. The amplitude variations in the frequency domain are much lower, and depend only on the chosen constellation. Therefore, we first transform the signal to the frequency domain and then we divide the signal at each subcarrier by $s[k]$ to avoid noise amplification by direct division. The resulting estimated EIR frequency response is then converted back to time domain, such that we have an estimate of the EIR $\hat{h}[l]$.

For radar range detection, we can then verify whether there is a target at the l -th range bin, corresponding to the l -th sample of the estimated EIR, by comparing the value of its amplitude with a given threshold λ_l , i.e.,

$$\left| \hat{h}[l] \right| \underset{H_0}{\overset{H_1}{\gtrless}} \lambda_l, \quad (7)$$

with H_0 the null hypothesis and H_1 the hypothesis that there is an object in the l -th range bin. The dependency of λ_l on l means that the threshold may vary depending on the range bin, to have a constant false alarm rate (CFAR).

We will now represent the system in matrix notation.

1) *Signal Model:* Suppose there are G samples in the GI. Let us represent the EIR as a column vector of arbitrary complex scattering coefficients that is given by

$$\mathbf{h} := [h[l]]_{l=0}^{G-1} \in \mathbb{C}^G. \quad (8)$$

In order to represent the convolution of the transmit signal and the EIR, in the sequel, we define a Toeplitz matrix. A Toeplitz matrix is a matrix where each descending diagonal from left to right is constant, meaning that the matrix elements remain constant along diagonals that are parallel to the main diagonal. This specific property is particularly useful for analyzing incident waveforms in multipath scenarios, where the waveform can be represented as a convolution with local ambient scattering. Thus, the ambient scattering in the surrounding area can be modeled using a Toeplitz matrix, allowing an efficient analysis of the incident waveform [30].

Let $P := N + G$, be the number of data samples in the whole OFDM symbol including the GI. We define a Toeplitz matrix \mathbf{H} such that

$$\mathbf{H} := \text{Toep}([h^T \mathbf{0}_{1 \times N}]^T, :) \in \mathbb{C}^{P \times P}. \quad (9)$$

Now let us write the data in vector format:

$$\mathbf{s} := [s[k]]_{k=0}^{N-1} \in \mathbb{C}^N, \quad (10)$$

and

$$\mathbf{F}_N := [e^{-j\omega ln}]_{l=0, n=0}^{N-1, N-1}, \text{ with } \omega := 2\pi/N, \quad (11)$$

be the discrete Fourier transform (DFT) matrix, usually implemented as a fast Fourier transform (FFT), with $\mathbf{F}_N \mathbf{F}_N^H = N \mathbf{I}_N$ property. We drop the index N when the size of FFT is clear from the context. The time-domain samples of the transmit signal after the IFFT are given by

$$\mathbf{x} := \mathbf{F}^H \mathbf{s} \in \mathbb{C}^N. \quad (12)$$

After removing the CP at the receiver, the EIR matrix becomes a circular matrix, with the following model for the received signal,

$$\mathbf{y} = \mathbf{H}_{\text{cir}} \mathbf{x} + \mathbf{w} \in \mathbb{C}^N, \quad (13)$$

where $\mathbf{H}_{\text{cir}} = \text{Circ}([\mathbf{h}^\top \mathbf{0}_{1 \times (N-G)}]^\top) \in \mathbb{C}^{N \times N}$.

2) *Range Estimation and Target Detection for CP-OFDM-JCAS*: The receiver benefits from an element-wise division of the Fourier transform of the received signal by the frequency-domain transmit symbols. Using IFFT, it is simple to estimate the EIR in vector format, such that

$$\hat{\mathbf{h}} = \mathbf{F}^H ((\mathbf{F}\mathbf{y}) \odot \mathbf{s}^{-1}) / N^2 \in \mathbb{C}^N, \quad (14)$$

where $\hat{\mathbf{h}}$ has the EIR estimate \mathbf{h} on its first G elements. To enhance the SNR in CP-OFDM, the receiver can integrate the outcomes of M pulses, either coherently or incoherently. We will discuss it later in analytical result section.

Finally, applying the detector (7) over the elements of $\hat{\mathbf{h}}$ provides the range detection.

Doppler estimation: In CP-OFDM, the modulation symbols on a fixed subcarrier index are subject to a Doppler shift, leading to a linear phase shift between them. To determine the Doppler shift, one can perform an FFT on the slow-time samples of each subcarrier, as stated in [15].

C. Signal and System Model for ZP-OFDM-JCAS

Instead of the more common CP-OFDM, we proposed in [28] to use ZP-OFDM, where the transmitter remains idle during the GI between every OFDM symbol (see Fig. 5). During the silence time interval, the transceiver can be switched from transmit to radar-detection mode. Furthermore, there will be no SI to radar signal during this period. However, we cannot make use of the full reflected wave, but only of its part that falls within the GI. We showed that the proposed waveform outperforms CP-OFDM at full-duplex mode if there is low isolation between transmitter and receiver, particularly for long-ranges. The transmit signal model and the required signal processing for radar detection are presented in the following.

1) *Signal Model*: The transmitter zero-pads \mathbf{x} by appending G null samples, i.e., the full symbol is given by

$$\mathbf{x}_{\text{zp}} := [\mathbf{x}^\top \mathbf{0}_{1 \times G}]^\top \in \mathbb{C}^P, \quad (15)$$

and let $\tilde{\mathbf{x}} \in \mathbb{C}^G$ be the last G elements of \mathbf{x} ,

$$\tilde{\mathbf{x}}[i] := \mathbf{x}[N - G + i], \quad 0 \leq i \leq G - 1. \quad (16)$$

Then, the received signal at the GI takes the following form:

$$\tilde{\mathbf{y}} = \tilde{\mathbf{H}}\tilde{\mathbf{x}} + \tilde{\mathbf{w}} \in \mathbb{C}^G, \quad (17)$$

where

$$\tilde{\mathbf{H}} := \mathbf{H}[N+1:P, N-G+1:N], \quad (18)$$

which equivalently can be written as

$$\tilde{\mathbf{H}} = \text{Toep}(:, \tilde{\mathbf{h}}^\top) \in \mathbb{C}^{G \times G}, \quad (19)$$

where $\tilde{\mathbf{h}}$ is the flipped vector of \mathbf{h} , given by

$$\tilde{\mathbf{h}} = [h[G-1] \cdots h[0]]^\top \in \mathbb{C}^G, \quad (20)$$

and $\tilde{\mathbf{H}}$ is an upper-triangular Toeplitz matrix. The receiver estimates the EIR vector $\tilde{\mathbf{h}}$ from the echoes in $\tilde{\mathbf{y}}$, which corresponds to the G samples received in the GI. The following subsection elaborates a method to estimate $\tilde{\mathbf{h}}$ for range estimation.

2) *Range Estimation*: In ZP mode, the radar receiver only has access to the part of the signal that falls into the guard interval. As mentioned before, the integration over M pulses can be performed to compensate the SNR loss. Let \mathbf{x}_m denote the transmit signal at the m -th pulse. The receiver, first evaluates the EIR for the m -th pulse, and then integrate the estimates of

\mathbf{h}_m to benefit from integration gain. To include the slow-time pulse index, we modify (17) as

$$\tilde{\mathbf{y}}_m = \tilde{\mathbf{H}}_m \tilde{\mathbf{x}}_m + \tilde{\mathbf{w}}_m \in \mathbb{C}^G. \quad (21)$$

Our underlying assumption throughout this paper is that the Doppler is low enough, such that \mathbf{h}_m (equivalently $\tilde{\mathbf{h}}_m$) is fixed during transmission of M pulses, i.e., $\mathbf{h} = \mathbf{h}_m \forall m$ (equivalently $\tilde{\mathbf{H}} = \tilde{\mathbf{H}}_m \forall m$). Therefore, we reformulate (21) as

$$\tilde{\mathbf{y}}_m = \tilde{\mathbf{H}}\tilde{\mathbf{x}}_m + \tilde{\mathbf{w}}_m \in \mathbb{C}^G, \quad (22)$$

To delve further, we introduce the subsequent Lemma.

Lemma 1: One can prove the following equation:

$$\tilde{\mathbf{H}}\tilde{\mathbf{x}}_m = \mathbf{X}_m \mathbf{h} \in \mathbb{C}^G, \quad (23)$$

with

$$\mathbf{X}_m = \text{Toep}(:, \mathbf{z}_m^\top) \in \mathbb{C}^{G \times G}, \quad (24)$$

where \mathbf{z}_m is the vector of reverse order of the last G elements of \mathbf{x}_m , which is given by

$$\mathbf{z}_m[i] := \mathbf{x}_m[N - i - 1], \quad 0 \leq i \leq G - 1, \quad (25)$$

and \mathbf{h} comes from (8).

Proof: Using the definitions of $\tilde{\mathbf{H}}$, $\tilde{\mathbf{x}}$, \mathbf{X}_m , \mathbf{h} in (19), (16), (24), (8), respectively, it is easy to show that

$$\tilde{\mathbf{H}}\tilde{\mathbf{x}}_m = \mathbf{X}_m \mathbf{h} = \left[\sum_{i=0}^{G-l-1} \mathbf{x}_m[N-1-i] \mathbf{h}[i+l] \right]_{l=0}^{G-1} \in \mathbb{C}^G. \quad \square$$

Applying Lemma 1, we reformulate (22) at the m -th received pulse as

$$\tilde{\mathbf{y}}_m = \mathbf{X}_m \mathbf{h} + \tilde{\mathbf{w}}_m \in \mathbb{C}^G. \quad (26)$$

The receiver can estimate \mathbf{h} by minimum mean square error (MMSE) estimator as

$$\hat{\mathbf{h}}_m = \mathbf{A}_m \mathbf{y}_m \in \mathbb{C}^G,$$

$$\begin{aligned} \mathbf{A}_m &:= \mathbf{C}_h \mathbf{X}_m^H (\mathbf{X}_m^H \mathbf{C}_h \mathbf{X}_m + \mathbf{C}_w)^{-1} \\ &= (\mathbf{X}_m^H \mathbf{C}_w^{-1} \mathbf{X}_m + \mathbf{C}_h^{-1})^{-1} \mathbf{X}_m^H \mathbf{C}_w^{-1} \in \mathbb{C}^{G \times G}, \end{aligned} \quad (27)$$

with $\mathbf{C}_h = \mathbb{E}(\mathbf{h}\mathbf{h}^H)$ the EIR covariance matrix and \mathbf{C}_w denotes the noise covariance matrix. We assume that the EIR is deterministic for M number of pulses, since the statistics of the EIR is unknown, thus we have no prior knowledge about it and the covariance becomes infinite $\mathbf{C}_h = \infty$ or $\mathbf{C}_h^{-1} = 0$. We consider this identity in (27), we get

$$\mathbf{A}_m = (\mathbf{X}_m^H \mathbf{C}_w^{-1} \mathbf{X}_m)^{-1} \mathbf{X}_m^H \mathbf{C}_w^{-1}, \quad (28)$$

Assuming the noise samples are uncorrelated, i.e., $\mathbf{C}_w = \sigma_w^2 \mathbf{I}_Q$, \mathbf{A}_m becomes

$$\mathbf{A}_m = (\mathbf{X}_m^H \mathbf{X}_m)^{-1} \mathbf{X}_m^H \in \mathbb{C}^{G \times G}, \quad (29)$$

which is a zero-forcing (ZF) estimator. To highlight the reliance of \mathbf{A}_m on \mathbf{X}_m in (29), we use the notation $\mathbf{X}_m^\dagger := (\mathbf{X}_m^H \mathbf{X}_m)^{-1} \mathbf{X}_m^H \in \mathbb{C}^{G \times G}$ throughout the paper. The generation of \mathbf{X}_m from a random communication data payload can produce singular matrices for certain indices, which can impair the radar's performance. Nevertheless, the radar terminal can detect and remove these singular matrices by applying a filter that establishes a threshold on the ratio between the largest and smallest eigenvalues of $\mathbf{X}_m^H \mathbf{X}_m$, i.e., $\frac{\sigma_{\min}}{\sigma_{\max}} \leq 1$. This ratio is particularly important for short-range communication since there are fewer samples available for short-range in the GI (refer to Fig. 2). As a result, the nonuniform distribution of the singular

values of \mathbf{X}_m can have a more severe impact on short-range communication.

3) *Target Detection*: Coherent and incoherent integration are two methods used in radar signal processing to improve the detection of targets. Coherent integration refers to the process of combining multiple radar pulses including their phase relationship. This results in an increase in the SNR and can help detect weak targets in the presence of noise. The variable \hat{h}_i represents the outcome of combining M pulses at the i -th range bin. Based on the insights from [31], the expression for \hat{h}_i under coherent integration can be given by

$$\hat{h}_i = \sum_{m=1}^M \hat{\mathbf{h}}_m[i]. \quad (30)$$

On the other hand, incoherent integration is utilized to detect targets with high RCS and involves the merging of multiple radar pulses while disregarding the phase. The formula for \hat{h}_i in the case of incoherent integration can be derived as

$$\hat{h}_i = \sum_{m=1}^M |\hat{\mathbf{h}}_m[i]|. \quad (31)$$

For the aim of comparison, we study another incoherent integration as sum of magnitude-square of the decision variables $\hat{\mathbf{h}}_m[i]$ which is given by

$$\hat{h}_i = \sum_{m=1}^M |\hat{\mathbf{h}}_m[i]|^2, \quad (32)$$

We use a uniform notation of \hat{h}_i in all scenarios, as their identification can be inferred from the context. The receiver can detect the most dominant spikes, corresponding to the targets' ranges via detector (7).

III. PROPOSED ZERO-PADDED WAVEFORM

When the PAPR is high, there are significant fluctuations in amplitude. As a result, the side-lobe levels at the output of matched filter (MF)/ estimator can be elevated, as the powerful amplitude variations may potentially overlap and compete with the main-lobe. In radar applications, the optimal scenario is to achieve MF outputs with uniformly sized and minimal side-lobes. If the side-lobes are not well-controlled and contain multiple instances of high energy, false targets known as ghost targets may emerge. Consequently, the likelihood of a false alarm increases and the detection performance diminishes, especially in low SNR conditions.

It is important to recognize that achieving a low PAPR does not necessarily guarantee a small peak-to-side-lobe level ratio (PSLR) for a MF output. Designing for a small PSLR requires careful consideration and there is an extensive body of literature dedicated to this topic, such as [32], [33], [34]. In the following, we present a simple solution to high PAPR challenge of ZP-OFDM.

A. Solution to High PAPR is ZP-SC-FDMA-JCAS

The problem of “ \mathbf{X}_m should not be singular”, or, equivalently, “ $\tilde{\mathbf{x}}[i]$ should not be close to zero”, motivates us to propose SC-FDMA which is another well-known waveform, used especially in the uplink, where lower PAPR benefits the mobile terminal in terms of transmit power efficiency.

1) *Signal Model*: Subcarrier mapping techniques in SC-FDMA can be categorized into two main types: localized mapping and distributed mapping [35]. In contrast to consecutive subcarrier mapping, distributed mapping assigns FFT outputs to non-consecutive subcarriers throughout the bandwidth. The remaining subcarriers have zero amplitude. Interleaved SC-FDMA (IFDMA), as described in [35], is an example of distributed SC-FDMA where the occupied subcarriers are evenly spaced across the bandwidth.

In our study, we employed IFDMA to distribute N_1 data payloads over a total of N subcarriers. To simplify the formulation, we assume that the total number of subcarriers is $k + 1$ times greater than the number of data samples. To generate a symbol for SC-FDMA, the transmitted signal in the time domain \mathbf{s}_m undergoes an N_1 -point FFT, where $N > N_1$, (see Fig. 5), thus we have

$$\mathbf{a}_m := \mathbf{F}_{N_1} \mathbf{s}_m \in \mathbb{C}^{N_1}, \quad (33)$$

In the second stage, the SC-FDMA needs a subcarrier mapping matrix, i.e., \mathbf{M} , which maps \mathbf{a}_m into N subcarriers. Assume N is $k + 1$ times larger than N_1 , e.g., by mapping N_1 FFT points into N subcarriers with insertion of k zeros between them. The mapping matrix $\mathbf{M} \in \mathbb{R}^{N \times N_1}$ can be defined as follows

$$\tilde{\mathbf{s}}_m := \mathbf{M} \mathbf{a}_m \in \mathbb{C}^N,$$

$$\mathbf{M}[:, n] = \mathbf{e}_{n(k+1)+1} \in \mathbb{R}^N, \quad 0 \leq n \leq N_1 - 1. \quad (34)$$

Here, $\mathbf{M}[:, n]$ refers to the n -th column of matrix \mathbf{M} . Afterwards, the transmit signal can be obtained by performing an IFFT on the vector $\tilde{\mathbf{s}}_m$, which is given by

$$\mathbf{x}_m := \mathbf{F}_N^H \tilde{\mathbf{s}}_m \in \mathbb{C}^N. \quad (35)$$

Here, \mathbf{x}_m has a lower PAPR than \mathbf{x}_m of OFDM, because the symbols are first processed by an N_1 -point FFT [35], [36].

2) *Range Estimation and Target Detection*: The MMSE estimation procedure for ZP-OFDM-JRC outlined in Section II-C2 can be combined with the target detection procedure from Section II-C3 to enable the identification of targets and their corresponding ranges.

IV. DETECTION PERFORMANCE

The objective at the radar receiver is to identify the targets, and the choice of processing method depends on the receiver's characteristics. Initially, we'll examine the incoherent scenario, followed by coherent processing of all waveforms. This approach will provide a more clear understanding of why ZP-SC-FDMA outperforms ZP-OFDM in terms of radar detection performance.

A. Incoherent Processing

1) *ZP-Sequence*: We first examine the scenario where the target is detected at the i -th range bin, corresponding to the \mathcal{H}_1 hypothesis. Following that, we will consider the target-absent scenario, corresponding to the \mathcal{H}_0 hypothesis.

a) *Under \mathcal{H}_1 hypothesis*: The i -th bin of the estimated EIR can be given by

$$\hat{\mathbf{h}}_m[i] = \mathbf{h}_m[i] + \mathbf{X}_m^\dagger[i, :]^T \tilde{\mathbf{w}}_m, \quad (36)$$

where $\mathbf{X}_m^\dagger[i, :]$ represents the i -th row of \mathbf{X}_m^\dagger . Recall the assumption that the Doppler shift is slow enough not to change $\mathbf{h}_m[i]$ during M transmission, i.e., $\mathbf{h}[i] := \mathbf{h}_m[i]$,

$$\hat{\mathbf{h}}_m[i] = \mathbf{h}[i] + \mathbf{X}_m^\dagger[i, :]^T \tilde{\mathbf{w}}_m. \quad (37)$$

From now on, we simplify the notations as follows:

$$\begin{aligned}\mathbf{x}_{i,m}^\dagger &:= \mathbf{X}_m^\dagger[i, :] \in \mathbb{C}^G, \\ h_i &:= \mathbf{h}[i] \in \mathbb{C}, \\ \hat{h}_{i,m} &:= \hat{\mathbf{h}}_m[i] \in \mathbb{C}, \\ \mathbf{w}_m &:= \tilde{\mathbf{w}}_m,\end{aligned}\quad (38)$$

such that (37) can be rewritten as

$$\hat{h}_{i,m} = h_i + \mathbf{x}_{i,m}^\dagger \mathbf{w}_m. \quad (39)$$

Note that \dagger in $\mathbf{x}_{i,m}^\dagger$ is just a representation notation and it means $\mathbf{x}_{i,m}^\dagger$ comes from matrix $\mathbf{X}_m^\dagger[i, :]$. Assuming that the noise samples in \mathbf{w}_m are independent circularly symmetric complex Gaussian random variables, and by using the fact that the linear combination of normal variables are again normal, we can write

$$\begin{aligned}\operatorname{Re}\{\hat{h}_{i,m}\} &= \operatorname{Re}\{h_i + \mathbf{x}_{i,m}^{\dagger T} \mathbf{w}_m\} \sim \mathcal{N}\left(\operatorname{Re}\{h_i\}, \|\mathbf{x}_{i,m}^\dagger\|^2 \frac{\sigma_w^2}{2}\right), \\ \operatorname{Im}\{\hat{h}_{i,m}\} &= \operatorname{Im}\{h_i + \mathbf{x}_{i,m}^{\dagger T} \mathbf{w}_m\} \sim \mathcal{N}\left(\operatorname{Im}\{h_i\}, \|\mathbf{x}_{i,m}^\dagger\|^2 \frac{\sigma_w^2}{2}\right),\end{aligned}\quad (40)$$

where $\mathcal{N}(\mu, \sigma^2)$ is normal distribution with mean μ and variance σ^2 . In general, there are two methods to accumulate the pulses for incoherent integration, square-law and linear.

In the following we first use the sum of magnitude approach, thus the decision is based on the magnitude of $\hat{h}_{i,m}$,

$$|\hat{h}_{i,m}| = \sqrt{\operatorname{Re}^2\{\hat{h}_{i,m}\} + \operatorname{Im}^2\{\hat{h}_{i,m}\}} \sim \operatorname{Rice}(\mu_i, \sigma_{i,m}), \quad (41)$$

$$\mu_i := |h_i|,$$

$$\sigma_{i,m} := \frac{\|\mathbf{x}_{i,m}^\dagger\| \sigma_w}{\sqrt{2}}. \quad (42)$$

The Rice distribution in (41) has the following mean and variance,

$$\begin{aligned}\tilde{\eta}_{i,m} &= \sigma_{i,m} \sqrt{\pi/2} L_{1/2}(\gamma_{i,m}), \\ \tilde{\sigma}_{i,m}^2 &= 2\sigma_{i,m}^2 + \mu_i^2 - \frac{\pi\sigma_{i,m}^2}{2} L_{1/2}^2(\gamma_{i,m}),\end{aligned}\quad (43)$$

where

$$\gamma_{i,m} := \frac{-\mu_i^2}{2\sigma_{i,m}^2} = \frac{-|h_i|^2}{\sqrt{2}\|\mathbf{x}_{i,m}^\dagger\|^2 \sigma_w^2} \quad (44)$$

is the shaping factor and

$$L_{1/2}(\gamma) := e^{\gamma/2} \left[(1-\gamma) \mathcal{I}_0\left(-\frac{\gamma}{2}\right) - \gamma \mathcal{I}_1\left(-\frac{\gamma}{2}\right) \right]. \quad (45)$$

Approximation using CLT: In order to make the analysis tractable, we approximate the distribution of the sum of Rician random variables using the central limit theorem (CLT), i.e., in case of accumulating M pulses when M is large enough, we get the sum of means and variances of each variable, which is given by

$$\begin{aligned}\hat{h}_i &:= \sum_{m=1}^M |\hat{h}_{i,m}| \sim \mathcal{N}(\eta_{1,i}, \sigma_{1,i}^2), \\ \eta_{1,i} &:= \sum_{m=1}^M \tilde{\eta}_{i,m},\end{aligned}$$

$$\sigma_{1,i}^2 := \sum_{m=1}^M \tilde{\sigma}_{i,m}^2. \quad (46)$$

The subscript ‘1’ in mean and variance represents the \mathcal{H}_1 hypothesis.

b) Under \mathcal{H}_0 hypothesis: In this case, $h_i = 0$, and (40) turns into the following form,

$$\begin{aligned}\operatorname{Re}\{\hat{h}_{i,m}\} &= \operatorname{Re}\{\mathbf{x}_{i,m}^{\dagger T} \mathbf{w}_m\} \sim \mathcal{N}\left(0, \|\mathbf{x}_{i,m}^\dagger\|^2 \frac{\sigma_w^2}{2}\right), \\ \operatorname{Im}\{\hat{h}_{i,m}\} &= \operatorname{Im}\{\mathbf{x}_{i,m}^{\dagger T} \mathbf{w}_m\} \sim \mathcal{N}\left(0, \|\mathbf{x}_{i,m}^\dagger\|^2 \frac{\sigma_w^2}{2}\right),\end{aligned}\quad (47)$$

and the decision variable $|\hat{h}_{i,m}|$ has a Rayleigh distribution, with mean and variance

$$|\hat{h}_{i,m}| \sim \operatorname{Rayleigh}(\sigma_{i,m}), \quad (48)$$

and $\sigma_{i,m}$ comes from (42). The Rayleigh distribution in (48) has the following mean and variance,

$$\begin{aligned}\check{\eta}_{i,m} &:= \sigma_{i,m} \sqrt{\pi/2}, \\ \check{\sigma}_{i,m}^2 &:= 2\sigma_{i,m}^2 - \frac{\pi}{2}\sigma_{i,m}^2,\end{aligned}\quad (49)$$

and, by accumulating M pulses, also based on the CLT, we get the sum of means and variances given by

$$\begin{aligned}\hat{h}_i &:= \sum_{m=1}^M |\hat{h}_{i,m}| \sim \mathcal{N}(\eta_{0,i}, \sigma_{0,i}^2), \\ \eta_{0,i} &:= \sum_{m=1}^M \check{\eta}_{i,m}, \\ \sigma_{0,i}^2 &:= \sum_{m=1}^M \check{\sigma}_{i,m}^2.\end{aligned}\quad (50)$$

The subscript ‘0’ in mean and variance represents the \mathcal{H}_0 hypothesis.

c) Neyman-Pearson detector: The detection of the targets can be performed by NP (Neyman-Pearson) test, using the results in (46) and (50),

$$\hat{h}_i \sim \begin{cases} \mathcal{N}(\eta_{1,i}, \sigma_{1,i}^2), & \text{under } \mathcal{H}_1 \\ \mathcal{N}(\eta_{0,i}, \sigma_{0,i}^2), & \text{under } \mathcal{H}_0. \end{cases}$$

Note that here the decision variable is a real number.

Lemma 2 (ROC): For a real variable, i.e., \hat{h}_i , the relationship between probability of detection p_d and probability of false alarm p_{fa} can be calculated with some elementary math. Let λ be the threshold, then we obtain

$$\begin{aligned}p_{fa} &= p(\hat{h}_i > \lambda | \mathcal{H}_0) = \mathcal{Q}\left(\frac{\lambda - \eta_0}{\sigma_0}\right), \\ p_d &= p(\hat{h}_i > \lambda | \mathcal{H}_1) = \mathcal{Q}\left(\frac{\lambda - \eta_1}{\sigma_1}\right) \\ &= \mathcal{Q}\left(\frac{\sigma_0 \mathcal{Q}^{-1}(p_{fa}) + \eta_0 - \eta_1}{\sigma_1}\right).\end{aligned}\quad (51)$$

Here we dropped the index i for notational simplicity.

Approximation of p_d at high SNR regime: To be able to obtain p_d analytically, we consider only the high SNR case, when the shaping factor of the Rice distribution is negative and large, i.e.,

$\gamma_{i,m}$, which means

$$-\gamma_{i,m} = \frac{|h_i|^2}{\sqrt{2}\|\mathbf{x}_{i,m}^\dagger\|^2\sigma_w^2} = c, \quad c \gg 0, \quad (52)$$

we use the identity $\lim_{\gamma \rightarrow -\infty} L_{1/2}(\gamma) = |\gamma|^{1/2}/\Gamma(3/2)$ to simplify the variance of the Rice distribution, such that

$$\begin{aligned} \lim_{\gamma_{i,m} \rightarrow -\infty} L_{1/2}(\gamma_{i,m}) &= |\gamma_{i,m}|^{1/2}/\Gamma(3/2) \\ &= \frac{\sqrt{2}|h_i|}{\sqrt{\pi}\sigma_{i,m}} = \frac{2|h_i|}{\sqrt{\pi}\|\mathbf{x}_{i,m}^\dagger\|\sigma_w}. \end{aligned} \quad (53)$$

We use (53) to prove the following theorem about ZP-sequences.

Theorem 1 (ZP-sequences with incoherent integration): The probability of detection at high SNR at the radar terminal is approximated by

$$p_d \approx \mathcal{Q}(\alpha\mathcal{Q}^{-1}(p_{fa}) + \beta_i) \quad (54)$$

with

$$\alpha := \sqrt{1 - \pi/4}, \quad (55)$$

$$\beta_i := \frac{\sqrt{\pi}/2 \sum_{m=1}^M \|\mathbf{x}_{i,m}^\dagger\|\sigma_w - M|h_i|}{(\sum_{m=1}^M \|\mathbf{x}_{i,m}^\dagger\|^2)^{1/2}\sigma_w}. \quad (56)$$

Proof: α is the ratio between the two standard deviations of both hypotheses, i.e., $\frac{\sigma_0}{\sigma_1}$ and can be calculated as (55). To obtain

β_i , we need to calculate $\beta_i := \frac{\eta_0 - \eta_1}{\sigma_1}$, so we start with the numerator such that

$$\begin{aligned} \eta_0 - \eta_1 &= \sum_{m=1}^M (\tilde{\eta}_{i,m} - \tilde{\eta}_{i,m}) \\ &= \sum_{m=1}^M \sigma_{i,m} \sqrt{\pi/2} \left(1 - \lim_{\gamma_{i,m} \rightarrow -\infty} L_{1/2}(\gamma_{i,m}) \right) \\ &= \sum_{m=1}^M \sigma_{i,m} \sqrt{\pi/2} \left(1 - \frac{\sqrt{2}|h_i|}{\sqrt{\pi}\sigma_{i,m}} \right), \end{aligned} \quad (57)$$

Now, β_i is

$$\begin{aligned} \beta_i &= \frac{\sum_{m=1}^M \sigma_{i,m} \sqrt{\pi/2} \left(1 - \frac{\sqrt{2}|h_i|}{\sqrt{\pi}\sigma_{i,m}} \right)}{(2 \sum_{m=1}^M \sigma_{i,m}^2)^{1/2}} \\ &= \frac{\sqrt{\pi/2} \sum_{m=1}^M \sigma_{i,m} - M|h_i|}{(2 \sum_{m=1}^M \sigma_{i,m}^2)^{1/2}} \\ &= \frac{\sqrt{\pi}/2 \sum_{m=1}^M \|\mathbf{x}_{i,m}^\dagger\|\sigma_w - M|h_i|}{(\sum_{m=1}^M \|\mathbf{x}_{i,m}^\dagger\|^2)^{1/2}\sigma_w} \end{aligned} \quad (58)$$

and this completes the proof. \square

Discussion: It is clear from (56) that β_i is composed of two factors, let call them

$$\beta_i^{(1)} := \frac{\sqrt{\pi}/2 \sum_{m=1}^M \|\mathbf{x}_{i,m}^\dagger\|}{(\sum_{m=1}^M \|\mathbf{x}_{i,m}^\dagger\|^2)^{1/2}} \quad (59)$$

and

$$\beta_i^{(2)} := \frac{-M\gamma_i}{(\sum_{m=1}^M \|\mathbf{x}_{i,m}^\dagger\|^2)^{1/2}}, \quad (60)$$

with

$$\gamma_i := \frac{|h_i|}{\sigma_w}. \quad (61)$$

The first term $\beta_i^{(1)}$ is a positive upper-bounded quantity, since it has sum of the norms for the i -th range bin in both numerator and denominator. However, the limiting factor for p_d is the second term $\beta_i^{(2)}$. It may degrade the performance, since a large norm, i.e., $\|\mathbf{x}_{i,m}^\dagger\|$ can come into denominator. We explain this issue in more details in the next part as Remark 1. ZP-SC-FDMA has a lower PAPR in contrast to PAPR of ZP-OFDM. This characteristic makes SC-FDMA a suitable candidate for radar processing with zero padding. It is shown later that a high PAPR in the signal is a limiting factor for the radar performance.

d) Challenge of high norm for $\mathbf{x}_{i,m}^\dagger$: we analyse the issue of large norm for $\mathbf{x}_{i,m}^\dagger$ here to understand the dependency of radar performance to the proposed waveforms.

We consider the following form for singular value decomposition of \mathbf{X}_m ,

$$\mathbf{X}_m = \mathbf{U}_m \mathbf{\Sigma}_m \mathbf{V}_m^H \in \mathbb{C}^{G \times G}, \quad (62)$$

We may write

$$\begin{aligned} \|\mathbf{x}_{i,m}^\dagger\|^2 &= \left[\mathbf{X}_m^\dagger \mathbf{X}_m^H \right]_{i,i} \\ &= \left[(\mathbf{X}_m^H \mathbf{X}_m)^{-1} \mathbf{X}_m^H \mathbf{X}_m (\mathbf{X}_m^H \mathbf{X}_m)^{-1H} \right]_{i,i} \\ &= \left[(\mathbf{X}_m^H \mathbf{X}_m)^{-1} \right]_{i,i} = \left[(\mathbf{V}_m \mathbf{\Sigma}_m \mathbf{U}_m^H \mathbf{U}_m \mathbf{\Sigma}_m \mathbf{V}_m^H)^{-1} \right]_{i,i} \\ &= \left[\mathbf{V}_m^H \mathbf{\Sigma}_m^{-2} \mathbf{V}_m \right]_{i,i}, \end{aligned} \quad (63)$$

Let $\mathbf{v}_{i,m} := \mathbf{V}_m[:, i]$, and $\kappa_m[i]$ be the i -th singular value of \mathbf{X}_m , then

$$\|\mathbf{x}_{i,m}^\dagger\|^2 = \mathbf{v}_{i,m}^H \mathbf{\Sigma}_m^{-2} \mathbf{v}_{i,m} = \sum_{l=1}^G \kappa_m^{-2}[l] |\mathbf{v}_{i,m}[l]|^2. \quad (64)$$

This implies that if $\kappa_m[l]$ is tiny and $|\mathbf{v}_{i,m}[l]|^2$ is not small enough to compensate for a large $\kappa_m^{-2}[l]$, the norm $\|\mathbf{x}_{i,m}^\dagger\|^2$ gets very large, yielding the degradation of the detection performance. The next Lemma is important for understanding the connection between singular values of \mathbf{X}_m , i.e., $\kappa_m[l]$ and its spike samples. Before that, let us have the following definition.

Definition: The spike samples of upper-Toeplitz matrix $\mathbf{X}_m = \text{Toep}(\cdot, \mathbf{z}_m^\dagger) \in \mathbb{C}^{G \times G}$ with \mathbf{z}_m as its vector of construction can be given by

$$|\mathbf{z}_m[k]|^2 \gg \sum_{l=1}^G |\mathbf{z}_m[l]|^2 / G, \quad 1 \leq m \leq M, \quad (65)$$

which implies that the power of spike samples are far greater than the mean power.

Lemma 3: Let $\zeta_m[i]$ be the i -th eigenvalue of $\mathbf{X}_m^H \mathbf{X}_m$ and $\kappa_m[i]$ be the i -th singular value of \mathbf{X}_m , then $\zeta_m[i] = \kappa_m^2[i]$.

Proof: please refer to [37]. \square

$\mathbf{X}_m^H \mathbf{X}_m$ can be written as a sum of a diagonal matrix and another matrix, i.e., \mathbf{E}_m which contains just the off-diagonal elements of $\mathbf{X}_m^H \mathbf{X}_m$:

$$\mathbf{X}_m^H \mathbf{X}_m = \text{diag}(\zeta_m) + \mathbf{E}_m \in \mathbb{C}^{G \times G},$$

$$\zeta_m[i] := \sum_{l=1}^{G-i} |\mathbf{z}_m[l]|^2, \quad 0 \leq i \leq G-1, \quad (66)$$

Approximation of $\mathbf{X}_m^H \mathbf{X}_m$: Since \mathbf{X}_m is an upper-triangular-Toeplitz matrix, the off-diagonal elements of the product $\mathbf{X}_m^H \mathbf{X}_m$ are the inner product of two random sequences, and we may assume that they have very low correlation, given the fact that the data symbols are independent. By considering the off-diagonal elements to be negligible compared to the diagonal elements, which are sum of the powers of the signal samples, then $\mathbf{X}_m^H \mathbf{X}_m$ can be approximated by

$$\mathbf{X}_m^H \mathbf{X}_m \approx \text{diag}(\boldsymbol{\zeta}_m), \quad (67)$$

By applying Lemma 3, we have

$$\mathbf{X}_m^H \mathbf{X}_m \approx \text{diag}(\boldsymbol{\zeta}_m) = \text{diag}(\boldsymbol{\kappa}_m^2), \quad (68)$$

with

$$\boldsymbol{\kappa}_m^2 \approx \left[\sum_{l=1}^G |\mathbf{z}_m[l]|^2, \dots, |\mathbf{z}_m[2]|^2 + |\mathbf{z}_m[1]|^2, |\mathbf{z}_m[1]|^2 \right]. \quad (69)$$

We use this fact and the observation of higher PAPR for ZP-OFDM to make the following statements on the radar performance.

Remark 1 (ZP-OFDM deteriorates the performance due to high PAPR): In case of ZP-OFDM, one or many samples may have large instantaneous power $|\mathbf{z}_m[l]|^2$. Assuming without loss of generality that the power of the J -th sample is significantly higher than the mean power. This implies that $\boldsymbol{\kappa}_m[j]$, $0 \leq j \leq J$ are also large due to (69). Since total power of the samples is fixed, this makes the other $\boldsymbol{\kappa}_m[j]$, $J+1 \leq j \leq G$ small. Those small singular values have the chance to make $\|\mathbf{x}_{i,m}^\dagger\|^2 = \sum_{l=1}^G \boldsymbol{\kappa}_m^{-2}[l] |\mathbf{v}_{i,m}[l]|^2$ very large. This implies that the argument $\frac{-M\gamma_i}{(\sum_{m=1}^M \|\mathbf{x}_{i,m}^\dagger\|^2)^{1/2}}$ of \mathcal{Q} function becomes less negative and the probability of detection goes down.

Remark 2: The samples $\mathbf{z}_m[l]$ with relative large powers (spike samples) occurred at the start of transmit symbols have their effect spread over all other samples afterwards, making them small due to a total fixed average transmit power. Consequently, the negative impact on p_d is by both the time of occurrence of those spike samples and the number of them.

2) *ZP-Sequences; Square-Law Detector:* In this section, we study the performance of ZP-sequences for incoherent processing with square-law detector. Before, we need the following Lemma assisting us to present the results.

Lemma 4: The decision variable h_i follows the pdf below for null and alternative hypotheses.

$$h_i \sim \begin{cases} \chi_\nu^2(\xi_i), & \text{under } \mathcal{H}_1 \\ \chi_\nu^2, & \text{under } \mathcal{H}_0. \end{cases}$$

Let $\mathcal{Q}_{\chi_\nu^2}$ denote the area under the right tail of chi-squared function with degree ν . Then, the following relationships between p_d and p_{fa} can be achieved:

$$\begin{aligned} p_{fa} &= p(h_i > \lambda; \mathcal{H}_0) = \mathcal{Q}_{\chi_\nu^2}(\lambda), \\ p_d &= p(h_i > \lambda; \mathcal{H}_1) = \mathcal{Q}_{\chi_\nu^2(\xi_i)}(\lambda) = \mathcal{Q}_{\chi_\nu^2(\xi_i)}(\mathcal{Q}_{\chi_\nu^2}^{-1}(p_{fa})) \\ &= \mathcal{Q}_{\nu/2} \left(\sqrt{\xi_i}, \sqrt{\mathcal{Q}_{\chi_\nu^2}^{-1}(p_{fa})} \right). \end{aligned} \quad (70)$$

Proof: Please refer to [38]. \square

By increasing the non-centrality parameter $M^2|h_i|^2$, the maximum of $\mathcal{Q}_{\chi_\nu^2(M^2|h_i|^2)}(\lambda)$ moves to the right and the right tail of

the distribution becomes larger, which means higher p_d for the same p_{fa} .

Theorem 2 (ZP-sequences with incoherent integration; square-law detector): The probability of detection for ZP-sequences with incoherent integration at the radar terminal is given by

$$p_d = Q_M \left(\sqrt{\xi_{zp}^{\text{inc}}[i]}, \sqrt{\mathcal{Q}_{\chi_{2M}^2}^{-1}(p_{fa})} \right), \quad (71)$$

with

$$\xi_{zp}^{\text{inc}}[i] = \gamma_i^2 \sum_{m=1}^M \frac{1}{\mathbf{v}_{i,m}^H \boldsymbol{\Sigma}_m^{-2} \mathbf{v}_{i,m}}. \quad (72)$$

Proof: We consider both hypotheses, starting with \mathcal{H}_1 .

• under \mathcal{H}_1 hypothesis we write

$$\begin{aligned} \hat{\mathbf{h}}_m[i] &= h_i + \mathbf{x}_{i,m}^{\dagger T} \mathbf{w}_m \sim \mathcal{CN}(h_i, \|\mathbf{x}_{i,m}^\dagger\|^2 \sigma_w^2), \\ \sigma_h^2(m, i) &:= \|\mathbf{x}_{i,m}^\dagger\|^2 \sigma_w^2, \\ \frac{\hat{\mathbf{h}}_m[i]}{\sigma_h(m, i)} &\sim \mathcal{CN} \left(\frac{h_i}{\sigma_h(m, i)}, 1 \right), \\ \hat{h}_{i,m} &:= \frac{|\hat{\mathbf{h}}_m[i]|^2}{\sigma_h^2(m, i)} \sim \chi_2^2 \left(\frac{|h_i|^2}{\sigma_h^2(m, i)} \right), \end{aligned} \quad (73)$$

We add M pulses incoherently with normalization by their variances,

$$\begin{aligned} \hat{h}_i &:= \sum_{m=1}^M \hat{h}_{i,m} \\ \hat{h}_i &\sim \chi_{2M}^2(\xi_{zp}^{\text{inc}}[i]), \\ \text{with } \xi_{zp}^{\text{inc}}[i] &:= \sum_{m=1}^M |\mu_{i,m}|^2 = \sum_{m=1}^M \frac{|h_i|^2}{\sigma_h^2(m, i)} \\ &= \frac{|h_i|^2}{\sigma_w^2} \sum_{m=1}^M \frac{1}{\|\mathbf{x}_{i,m}^\dagger\|^2} \\ &\stackrel{(a)}{=} \gamma_i^2 \sum_{m=1}^M \frac{1}{\mathbf{v}_{i,m}^H \boldsymbol{\Sigma}_m^{-2} \mathbf{v}_{i,m}}. \end{aligned} \quad (74)$$

where (a) equality is due to (61) and (64).

• under \mathcal{H}_0 hypothesis, we have

$$\begin{aligned} \hat{\mathbf{h}}_m[i] &= \mathbf{x}_{i,m}^{\dagger T} \mathbf{w} \sim \mathcal{CN}(0, \sigma_h^2(m, i)), \\ \hat{h}_{i,m} &:= \frac{|\hat{\mathbf{h}}_m[i]|^2}{\sigma_h^2(m, i)} \sim \chi_2^2, \end{aligned} \quad (75)$$

because σ_h^2 is known, we can normalize $|\hat{h}_i|^2$, such that

$$\begin{aligned} \hat{h}_i &:= \sum_{m=1}^M \hat{h}_{i,m}, \\ \hat{h}_i &\sim \chi_{2M}^2, \end{aligned} \quad (76)$$

$$\hat{h}_i \sim \begin{cases} \chi_{2M}^2(\xi_{zp}^{\text{inc}}[i]), & \text{under } \mathcal{H}_1 \\ \chi_{2M}^2, & \text{under } \mathcal{H}_0. \end{cases} \quad (77)$$

By applying Lemma 4, we achieve (71) in the theorem which completes the proof. \square

3) *CP-OFDM; Incoherent Detection:* In this section, we investigate the CP-OFDM with incoherent detection. We can

estimate the EIR as following,

$$\begin{aligned}\hat{\mathbf{h}}_m &= \mathbf{F}^H ((\mathbf{F}\mathbf{y}_m) \odot \mathbf{s}_m^{-1}) \\ &= \mathbf{h}_z + \mathbf{F}^H ((\mathbf{F}\mathbf{w}_m) \odot \mathbf{s}_m^{-1}) / N^2 \in \mathbb{C}^N, \\ \mathbf{h}_z &:= [\mathbf{h}^T \mathbf{0}_{1 \times (N-G)}]^T,\end{aligned}\quad (78)$$

The i -th range bin takes the following form,

$$\begin{aligned}\hat{\mathbf{h}}_m[i] &= h_i + \tilde{\mathbf{w}}_m[i], \\ \tilde{\mathbf{w}}_m[i] &:= \mathbf{F}^H [i, :] ((\mathbf{F}\mathbf{w}_m) ./ \mathbf{s}_m) / N^2,\end{aligned}\quad (79)$$

where $\mathbf{F}[i, :]$ means the i -th row and all columns of \mathbf{F} . To further simplify the notation, we define \mathbf{f}_i as the i -th row of the FFT matrix,

$$\mathbf{f}_i = \mathbf{F}[i, :]^T \in \mathbb{C}^{N \times 1}, \quad (80)$$

Considering (80), we reformulate (79) as

$$\begin{aligned}\tilde{\mathbf{w}}_m[i] &= \frac{1}{N^2} \mathbf{f}_i^H ((\mathbf{F}\mathbf{w}_m) \odot \mathbf{s}_m^{-1}) \\ &= \frac{1}{N^2} \mathbf{f}_i^H \text{diag}(\mathbf{s}_m^{-1}) \mathbf{F}\mathbf{w}_m,\end{aligned}\quad (81)$$

We define $\mathbf{a}_{i,m}$ to further simplify $\tilde{\mathbf{w}}_m[i]$ which is given by

$$\mathbf{a}_{i,m} := \frac{1}{N^2} \mathbf{f}_i^H \text{diag}(\mathbf{s}_m^{-1}) \mathbf{F}, \quad (82)$$

Thus by considering (82), we can write (81) as follow

$$\tilde{\mathbf{w}}_m[i] = \mathbf{a}_{i,m} \mathbf{w}_m \sim \mathcal{N}(0, \|\mathbf{a}_{i,m}\|^2 \sigma_w^2), \quad (83)$$

Lemma 5: Considering (82), we have the following identity for $\|\mathbf{a}_{i,m}\|^2$,

$$\|\mathbf{a}_{i,m}\|^2 = N^{-2} \forall i, m \quad (84)$$

Proof: We calculate $\|\mathbf{a}_{i,m}\|^2$ as follow

$$\begin{aligned}\|\mathbf{a}_{i,m}\|^2 &= \frac{1}{N^4} \|\mathbf{f}_i^H \text{diag}(\mathbf{s}_m^{-1}) \mathbf{F}\|^2 \\ &= \frac{1}{N^4} (\mathbf{f}_i^H \text{diag}(\mathbf{s}_m^{-1}) \mathbf{F}) (\mathbf{F}^H \text{diag}(\mathbf{s}_m^{-1})^H \mathbf{f}_i) = \frac{1}{N^2},\end{aligned}\quad (85)$$

in which we have used the following identities:

$$\begin{aligned}\text{diag}(|\mathbf{s}_m|^{-2}) &= \mathbf{I}_N, \\ \mathbf{F}\mathbf{F}^H &= N\mathbf{I}_N.\end{aligned}\quad (86)$$

This completes the proof. \square

We will use Lemma 5 in proofs of Theorems 3 and 5 for CP-OFDM. Now, we are ready to propose the following theorem about CP-OFDM with incoherent integration.

Theorem 3 (CP-OFDM with incoherent integration): The probability of detection for CP-OFDM with incoherent integration of M pulses at the radar terminal is given by

$$p_d = Q_M \left(\sqrt{\xi_{\text{cp}}^{\text{inc}}[i]}, \sqrt{Q_{\chi^2_{2M}}^{-1}(p_{fa})} \right) \quad (87)$$

where

$$\xi_{\text{cp}}^{\text{inc}}[i] = MN^2 \gamma_i^2 \forall i. \quad (88)$$

Proof: We consider two hypotheses below starting with \mathcal{H}_1 .

- under \mathcal{H}_1 hypothesis

$$\begin{aligned}\hat{\mathbf{h}}_m[i] &= h_i + \tilde{\mathbf{w}}_m[i] \sim \mathcal{CN}(h_i, \|\mathbf{a}_{i,m}\|^2 \sigma_w^2), \\ \sigma_h^2(i, m) &:= \|\mathbf{a}_{i,m}\|^2 \sigma_w^2, \\ \hat{h}_{i,m} &:= \frac{|\hat{\mathbf{h}}[i]|^2}{\sigma_h^2(i, m)} \sim \chi_{2M}^2 \left(\frac{|h_i|^2}{\sigma_h^2(i, m)} \right),\end{aligned}\quad (89)$$

We add M pulses incoherently with normalization by their variances,

$$\begin{aligned}\hat{h}_i &:= \sum_{m=1}^M \hat{h}_{i,m} \\ \hat{h}_i^{(1)} &\sim \chi_{2M}^2(\xi_{\text{cp}}^{\text{inc}}[i]), \\ \xi_{\text{cp}}^{\text{inc}}[i] &:= \sum_{m=1}^M \mu_{i,m}^2 = \sum_{m=1}^M \frac{|h_i|^2}{\sigma_h^2(m, i)} \\ &= \frac{|h_i|^2}{\sigma_w^2} \sum_{m=1}^M \frac{1}{\|\mathbf{f}_i^H \text{diag}(\mathbf{s}_m^{-1}) \mathbf{F}\|^2} = MN^2 \gamma_i^2,\end{aligned}\quad (90)$$

- under \mathcal{H}_0 hypothesis:

$$\hat{\mathbf{h}}_m[i] = \tilde{\mathbf{w}}_m[i] \sim \mathcal{CN}(0, \|\mathbf{a}_{i,m}\|^2 \sigma_w^2), \quad (91)$$

$\sigma_h^2(m, i)$ is known, so we normalize $|\hat{\mathbf{h}}_m[i]|^2$, such that

$$\begin{aligned}\hat{h}_{i,m} &:= \frac{|\hat{\mathbf{h}}_m[i]|^2}{\sigma_h^2(m, i)} \sim \chi_2^2, \\ \hat{h}_i &:= \sum_{m=1}^M \hat{h}_{i,m} \\ \hat{h}_i &\sim \chi_{2M}^2, \\ \hat{h}_i &\sim \begin{cases} \chi_{2M}^2(\xi_{\text{cp}}^{\text{inc}}[i]), & \text{under } \mathcal{H}_1 \\ \chi_{2M}^2, & \text{under } \mathcal{H}_0. \end{cases}\end{aligned}\quad (92)$$

The proof is concluded by utilizing Lemma 4 to obtain the results in (87). \square

B. Coherent Processing

This section aims to present two theorems that describe the performance of ZP-sequences and CP-OFDM in the case of coherent integration. However, prior to that, we will introduce Lemma 6, which provides the sufficient statistic for a complex normal binary hypothesis variable with an arbitrary variance. We will use this lemma in proving the theorems.

Lemma 6 (sufficient statistic): The sufficient statistic for NP detector of the following complex normal binary hypothesis variable with arbitrary $\sigma_h(i)$, i.e.,

$$\frac{\hat{h}_i}{\sigma_h(i)} \sim \begin{cases} \mathcal{CN}(Mh_i/\sigma_h(i), 1), & \text{under } \mathcal{H}_1 \\ \mathcal{CN}(0, 1), & \text{under } \mathcal{H}_0 \end{cases}$$

is $\frac{|\hat{h}_i|^2}{\sigma_h^2(i)}$.

Proof: Please see Appendix A. \square

1) *ZP-Sequences:* Now, we are ready to introduce the following theorem about probability of detection for ZP-sequences.

Theorem 4 (ZP-sequence with coherent integration): The probability of detection for ZP-sequences with coherent integration of M pulses at the radar terminal is given by

$$p_d = Q_1 \left(\sqrt{\xi_{\text{zp}}^{\text{coh}}[i]}, \sqrt{Q_{\chi^2_{2M}}^{-1}(p_{fa})} \right), \quad (93)$$

with

$$\xi_{\text{zp}}^{\text{coh}}[i] = \frac{M^2 \gamma_i^2}{\sum_{m=1}^M \sum_{q=1}^G \kappa_m^{-2}[q] |\mathbf{v}_{i,m}[q]|^2}, \quad (94)$$

where $Q_1(a, b)$ is the generalized Marcum Q-function of order 1, and γ_i comes from (61).

Proof: We examine two hypotheses, beginning with hypothesis \mathcal{H}_1 .

- under \mathcal{H}_1 hypothesis, we can write

$$\hat{\mathbf{h}}_m[i] = h_i + \mathbf{x}_{i,m}^{\dagger T} \mathbf{w}_m \sim \mathcal{CN}(\mathbf{h}[i], \|\mathbf{x}_{i,m}^{\dagger}\|^2 \sigma_w^2), \quad (95)$$

by integration of M pulses coherently, we get

$$\begin{aligned} \hat{h}_i &:= \sum_{m=1}^M \hat{\mathbf{h}}_m[i] = \sum_{m=1}^M h_i + \mathbf{x}_{i,m}^{\dagger T} \mathbf{w}_m \\ &= Mh_i + \sum_{m=1}^M \mathbf{x}_{i,m}^{\dagger T} \mathbf{w}_m, \end{aligned} \quad (96)$$

The pdf of the \hat{h}_i is given by

$$\hat{h}_i \sim \mathcal{CN}(Mh_i, \sigma_h^2(i)),$$

$$\text{with } \sigma_h^2(i) := \sum_{m=1}^M \|\mathbf{x}_{i,m}^{\dagger}\|^2 \sigma_w^2, \quad (97)$$

Since the variance is known, i.e., the noise variance can be estimated and transmit signal is known at the radar terminal, thus the pdf of the normalized variable is given by

$$\frac{\hat{h}_i}{\sigma_h(i)} \sim \mathcal{CN}\left(\frac{Mh_i}{\sigma_h(i)}, 1\right). \quad (98)$$

- under \mathcal{H}_0 hypothesis, we write

$$\begin{aligned} \hat{h}_i &:= \sum_{m=1}^M \hat{\mathbf{h}}_m[i] = \sum_{m=1}^M \mathbf{x}_{i,m}^{\dagger T} \mathbf{w}_m, \\ \hat{h}_i &\sim \mathcal{CN}\left(0, \sigma_h^2(i)\right), \end{aligned} \quad (99)$$

$\sigma_h^2(i)$ is known and can be calculated at the radar node by (97). By normalizing \hat{h}_i , we get

$$\frac{\hat{h}_i}{\sigma_h(i)} \sim \mathcal{CN}(0, 1), \quad (100)$$

and the binary hypothesis takes the following form

$$\frac{\hat{h}_i}{\sigma_h(i)} \sim \begin{cases} \mathcal{CN}(Mh_i/\sigma_h(i), 1), & \text{under } \mathcal{H}_1 \\ \mathcal{CN}(0, 1), & \text{under } \mathcal{H}_0 \end{cases}$$

with $\sigma_h(i)$ from (97). We use the sufficient statistic Lemma, i.e., Lemma 6, and the pdf of sufficient statistic variable for ZP-sequences which will be presented subsequently as Lemma 7, respectively. With the pdf at hand, the proof is concluded using Lemma 4. \square

The following Lemma yields the pdf of the sufficient statistic for ZP-sequences.

Lemma 7 (pdf of sufficient statistic variable for ZP-sequences): The pdf of the sufficient statistic variable of Lemma 6, i.e., $\frac{|\hat{h}_i|^2}{\sigma_h^2(i)}$ with $\sigma_h^2(i)$ obtained from (97), takes the following form

$$\frac{|\hat{h}_i|^2}{\sigma_h^2(i)} \sim \begin{cases} \chi_2^2(\xi_{zp}^{\text{coh}}[i]), & \text{under } \mathcal{H}_1 \\ \chi_2^2, & \text{under } \mathcal{H}_0, \end{cases} \quad (101)$$

with

$$\xi_{zp}^{\text{coh}}[i] = \frac{M^2 \gamma_i^2}{\sum_{m=1}^M \sum_{q=1}^G \kappa_m^{-2}[q] |\mathbf{v}_{i,m}[q]|^2}, \quad (102)$$

Proof: We calculate the pdf under both hypotheses as follows:

- under \mathcal{H}_1 hypothesis: the decision variable $\frac{|\hat{h}_i|^2}{\sigma_h^2(i)}$ is a non-central chi-squared which is given by

$$\frac{|\hat{h}_i|^2}{\sigma_h^2(i)} \sim \chi_2^2(\xi_{zp}^{\text{coh}}[i]), \quad (103)$$

with noncentrality parameter $\xi_{zp}^{\text{coh}}[i]$ which takes the following form

$$\xi_{zp}^{\text{coh}}[i] := \frac{M^2 |h_i|^2}{\sigma_h^2(i)} = \frac{M^2 |h_i|^2}{\sigma_w^2} \frac{1}{\sum_{m=1}^M \|\mathbf{x}_{i,m}^{\dagger}\|^2}, \quad (104)$$

considering (64), and $\gamma_i^2 = \frac{|h_i|^2}{\sigma_w^2}$ we write

$$\xi_{zp}^{\text{coh}}[i] = \frac{M^2 \gamma_i^2}{\sum_{m=1}^M \mathbf{v}_{i,m}^H \Sigma_m^{-2} \mathbf{v}_{i,m}}, \quad (105)$$

recall that $\kappa_m[i]$ is the i -th singular value of \mathbf{X}_m , and $\Sigma_m^{-2} = \text{diag}(\kappa_m^{-2})$ then we get the following expression

$$\xi_{zp}^{\text{coh}}[i] = \frac{M^2 \gamma_i^2}{\sum_{m=1}^M \sum_{q=1}^G \kappa_m^{-2}[q] |\mathbf{v}_{i,m}[q]|^2}, \quad (106)$$

- under \mathcal{H}_0 hypothesis, it is straightforward to show that

$$\frac{|\hat{h}_i|^2}{\sigma_h^2(i)} \sim \chi_2^2, \quad (107)$$

thus, the ultimate binary hypothesis is given by (101), thereby concluding the proof. \square

The following corollary shows how a small singular value can degrade the performance significantly.

Corollary 1: Assuming the p -th singular value of \mathbf{X}_m is small, i.e., $\kappa_m[p] \approx 0$ and it has the same value for M pulses, then this singular value will be dominant in the non-centrality parameter $\xi_{zp}^{\text{coh}}[i]$ calculation such that

$$\xi_{zp}^{\text{coh}}[i] = \frac{M^2 \gamma_i^2}{\sum_{m=1}^M \sum_{q=1}^G \kappa_m^{-2}[q] |\mathbf{v}_{i,m}[q]|^2} = \frac{M \gamma_i^2 \kappa_m^2[p]}{|\mathbf{v}_{i,m}[p]|^2} \approx 0. \quad (108)$$

and

$$p_d \approx Q_1\left(0, \sqrt{Q_{\chi_{2M}^2}^{-1}(p_{fa})}\right) = Q_{\chi_2^2(0)}\left(Q_{\chi_2^2}^{-1}(p_{fa})\right) = p_{fa}. \quad (109)$$

This implies that in the scenario of ZP-sequence with coherent integration, the presence of spike samples can result in an increase in the argument of the Q function (note this Q function is different from generalized Marcum Q-function), subsequently reducing the likelihood of detection p_d in cases where the false alarm probability p_{fa} is low, as indicated by the linear relationship in (109).

2) *CP-OFDM:* Assume N is the number of subcarriers and γ_i is the SNR of the i -th range bin, then we propose the next theorem for CP-OFDM with coherent integration.

Theorem 5 (CP-OFDM with coherent integration): The probability of detection for CP-OFDM with coherent integration of

M pulses at the radar terminal is given by

$$p_d = Q_1 \left(\sqrt{\xi_{\text{cp}}^{\text{coh}}[i]}, \sqrt{Q_{\chi_2^2}^{-1}(p_{fa})} \right) \quad (110)$$

where

$$\xi_{\text{cp}}^{\text{coh}}[i] = MN^2\gamma_i^2, \quad 0 \leq i \leq G-1. \quad (111)$$

Proof: similar to previous proofs, this one is also divided into two parts.

- under \mathcal{H}_1 hypothesis, the estimate of EIR corresponding to the i -th range bin with M integration can be given by

$$\hat{h}[i] := \sum_{m=1}^M \hat{\mathbf{h}}_m[i] = Mh_i + \sum_{m=1}^M \tilde{\mathbf{w}}_m[i]. \quad (112)$$

The pdf of $\hat{h}[i]$ takes the following form

$$\begin{aligned} \hat{h}[i] &\sim \mathcal{CN}(Mh_i, \sigma_h^2(i)), \\ \sigma_h^2(i) &:= \sum_{m=1}^M \|\mathbf{a}_{i,m}\|^2 \sigma_w^2 \stackrel{(a)}{=} \frac{M\sigma_w^2}{N^2}, \end{aligned} \quad (113)$$

where (a) equality comes from Lemma 5. Since $\sigma_h^2(i)$ is known at the receiver, it is possible to normalize $\hat{h}[i]$ such that

$$\frac{\hat{h}[i]}{\sigma_h(i)} \sim \mathcal{CN}\left(\frac{Mh_i}{\sigma_h(i)}, 1\right), \quad (114)$$

where \mathcal{CN} denotes the complex normal pdf.

- under \mathcal{H}_0 hypothesis:

$$\begin{aligned} \hat{h}[i] &:= \sum_{m=1}^M \tilde{\mathbf{w}}_m[i], \\ \hat{h}[i] &\sim \mathcal{CN}(0, \sigma_h^2(i)), \end{aligned} \quad (115)$$

by normalizing

$$\frac{\hat{h}[i]}{\sigma_h(i)} \sim \mathcal{CN}(0, 1), \quad (116)$$

and the binary hypothesis takes the following form

$$\frac{\hat{h}_i}{\sigma_h(i)} \sim \begin{cases} \mathcal{CN}(Mh_i/\sigma_h(i), 1), & \text{under } \mathcal{H}_1 \\ \mathcal{CN}(0, 1), & \text{under } \mathcal{H}_0, \end{cases}$$

where $\sigma_h(i)$ is presented in (113). By utilizing the sufficient statistic Lemma, namely Lemma 6 and the pdf of the sufficient statistic variable for ZP-sequences in Lemma 8 which comes in the sequel, we obtain the final decision variable and its probability density function, respectively. With the pdf available, the proof is completed by employing Lemma 4. \square

As stated in the concluding paragraph of the proof for Theorem 5, the following Lemma, namely Lemma 8, is utilized subsequent to Lemma 6 to introduce the pdf of the sufficient statistic variable in the CP-OFDM scenario.

Lemma 8 (pdf of sufficient statistic variable for CP-OFDM):

The pdf of the sufficient statistic $\frac{|\hat{h}_i|^2}{\sigma_h^2(i)}$ with $\sigma_h^2(i) = \frac{M\sigma_w^2}{N^2}$, for CP-OFDM, takes the following form

$$\frac{|\hat{h}_i|^2}{\sigma_h^2(i)} \sim \begin{cases} \chi_2'^2(\xi_{\text{cp}}^{\text{coh}}[i]), & \text{under } \mathcal{H}_1 \\ \chi_2^2, & \text{under } \mathcal{H}_0, \end{cases} \quad (117)$$

with $\xi_{\text{cp}}^{\text{coh}}[i] = MN^2\gamma_i^2$.

Proof: We calculate the pdf under both hypotheses as follows:

- under \mathcal{H}_1 hypothesis:

The normalized amplitude-squared has the noncentral chi-squared pdf with two degrees of freedom and noncentrality parameter $\xi_{\text{cp}}^{\text{coh}}[i]$ which is given by

$$\begin{aligned} \frac{|\hat{h}[i]|^2}{\sigma_h^2(i)} &\sim \chi_2'^2(\xi_{\text{cp}}^{\text{coh}}[i]), \\ \xi_{\text{cp}}^{\text{coh}}[i] &= \frac{M^2|h_i|^2}{\sigma_h^2[i]} \stackrel{(a)}{=} MN^2\gamma_i^2. \end{aligned} \quad (118)$$

We have used (113), for (a) equality.

- under \mathcal{H}_0 hypothesis:

$$\begin{aligned} \frac{\hat{h}[i]}{\sigma_h(i)} &\sim \mathcal{CN}(0, 1), \\ \frac{|\hat{h}[i]|^2}{\sigma_h^2(i)} &\sim \chi_2^2, \\ \frac{|\hat{h}[i]|^2}{\sigma_h^2(i)} &\sim \begin{cases} \chi_2'^2(\xi_{\text{cp}}^{\text{coh}}[i]), & \text{under } \mathcal{H}_1 \\ \chi_2^2, & \text{under } \mathcal{H}_0. \end{cases} \end{aligned} \quad (119)$$

This completes the proof. \square

Remark 3: Note the major differences in performance between CP-OFDM for coherent and incoherent integration. The first difference is the index M , in $Q_M(\cdot)$ for incoherent integration instead of 1 in $Q_1(\cdot)$ for coherent integration, which increases the p_d for incoherent integration. However, since the b term in $Q_{M_1}(a, b)$ is a decreasing function with the argument b , and considering the fact that $\sqrt{Q_{\chi_2^2, M}^{-1}(p_{fa})} > \sqrt{Q_{\chi_2^2}^{-1}(p_{fa})}$ for the same p_{fa} , it compensates the degradation of the lower index for coherent case, resulting in the coherent case outperforming the incoherent one.

3) *Communications Receiver With ZP-OFDM:* Communications with ZP-OFDM have already been addressed at [27]. Note that the communication channel should be modeled with a different notation from the EIR of radar, e.g., \mathbf{C} instead of \mathbf{H} , because the radar and communication receivers have different locations geometrically and will experience different fading components and power delay profiles. In general there are two methods for communications, one deals with channel matrix inversions and the alternative is a simpler method called OLA, which is a FFT-based method and does not require matrix inversion [27].

V. NUMERICAL RESULTS

In this section, we assess the radar detection capabilities of various techniques examined in Section IV. The communication efficacy of ZP-sequences has been extensively studied in prior literature [27], [29] and is beyond the scope of this paper.

All important parameters of the numerical simulation including the system and waveform parameters are listed in Table I. For simplicity, we assumed a single-target radar EIR model. Utilizing the parameters presented in Table I, the range-bin indices of 90, 80, and 60 correspond to a long-range, medium-range, and short-range target located at distances of 112.5 m, 100 m, and 75 m, respectively. To assess the performance of the suggested ZP waveforms against CP-OFDM, we generate an ROC curve solely for the coherent scenario, as the incoherent case exhibits a similar pattern. Additionally, we compare the numerical and analytical results to demonstrate that they mutually validate each other in this section.

We carried out the numerical simulation with $N_p = 10^6$ pulses for both target-absent and -present hypotheses. In order

TABLE I
SIMULATION PARAMETERS FROM 5 G NR [39]

parameter	value
carrier frequency	$f_c = 24$ GHz
bandwidth	$B = 400$ MHz
sample time	$t_{\text{sam}} = 1$ ns
subcarrier spacing	$\Delta f = 120$ KHz
# subcarriers	$N_c = 1024$
# cyclic prefix	$N_{\text{cp}} = 0.1N_c \approx 100$
symbol time	$t_{\text{sym}} = 8.33$ μs
cyclic prefix time	$t_{\text{cp}} = 0.1t_{\text{sym}} \approx 0.8$ μs
# zero-padded samples	$G = t_{\text{cp}}/t_{\text{sam}} = 800$
max. unambiguous range (CP-OFDM)	$ct_{\text{sym}}/2 \approx 1250$ m
max. unambiguous range (ZP-sequence)	$ct_{\text{cp}}/2 \approx 125$ m
# pulses	$N_p = 10^6$
# integrated pulses	$M = 10$
SNR at RX prior to pulse integration	20 dB
coherence interval	$t_{\text{ci}} = Mt_{\text{sym}} \approx 800$ μs
Doppler-frequency	10 kHz
# targets	1
RCS	1 m ²
# TX & # RX antennas	1 & 1
long & middle & short -range target	112.5 m & 100 m & 75 m
ADC resolution	10 bits

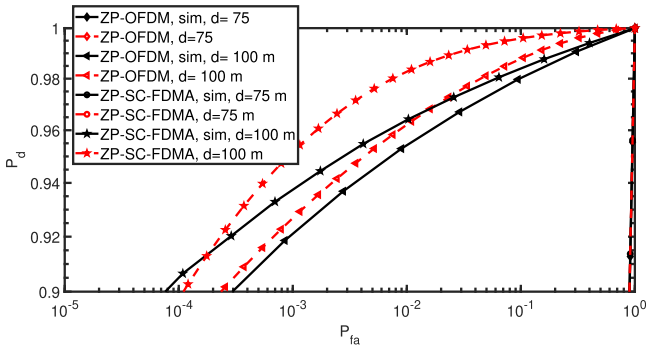


Fig. 6. The ROC curve illustrates a comparison between ZP-OFDM and ZP-SC-FDMA at 20 dB SNR with *coherent integration* for both analytical and simulated results. It also showcases how the performance of the considered waveforms is impacted by the range of the target.

to compare the performance, we utilize the estimators obtained from Section II for the range-bin associated with the target distance in both hypotheses. Subsequently, we plot the ROC curves for all the candidate waveforms, taking into account the various levels of isolation between the TX and RX. For the low and high isolation levels, we made the assumption of 10 dB and 50 dB transmit signal-to-self-interference power ratio (SSIR), respectively. Recall that the aim of the following subsection is to compare the different methods, and not how the same system performs in short and long ranges (Please refer to the discussions comes under Fig. 2).

A. Performance Comparison of ZP-Sequences for Various Ranges

The present section compared the detection performance of two potential zero-padding waveforms, namely ZP-SC-FDMA and ZP-OFDM, using both analytical and simulation approaches. The results are presented in Fig. 6. The superiority of ZP-SC-FDMA over ZP-OFDM in detection performance is consistently observed in both analytical and simulation results, as shown by the fact that the curve for ZP-SC-FDMA is always above that of ZP-OFDM. For instance, at a range of 100 m, the graph depicts that when the false alarm probability

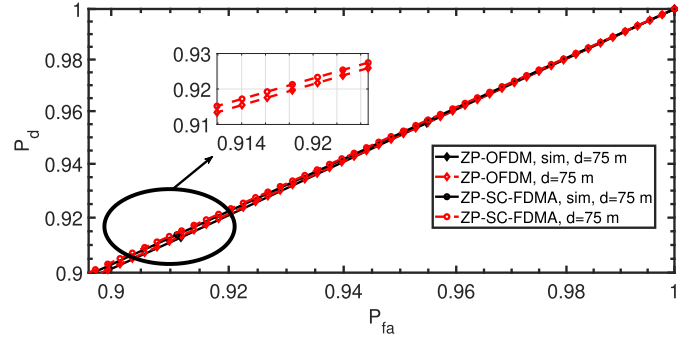


Fig. 7. The ROC plot illustrates the performance of ZP-sequences with coherent integration at 20 dB SNR. However, the results indicate that in short-range scenarios, such as 75 m, there are insufficient samples captured in the GI to achieve satisfactory detection performance when compared to long-range scenarios, as explained under the discussion of Fig. 2. To illustrate clear comparison between curves, only the analytical results are depicted in red color on the zoom-in diagram.

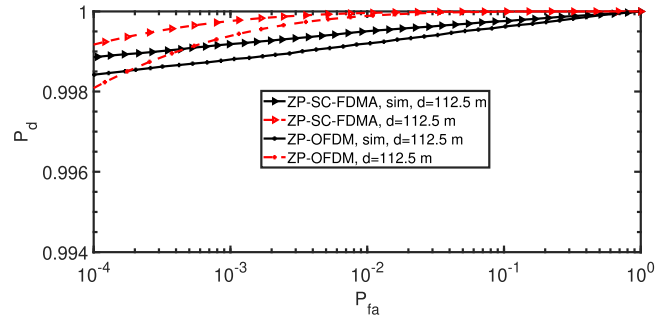


Fig. 8. The ROC plot for comparing ZP-OFDM and ZP-SC-FDMA with a 20 dB SNR at the receiver for coherent integration, for both analytical and simulation results. The plot is for a target located at 112.5 m.

is held constant at 10^{-3} , ZP-SC-FDMA achieves higher detection probabilities of 0.94, as compared to 0.92 for ZP-OFDM. The observed performance improvement aligns with Remark 1. Moreover, Fig. 6 exhibits a match between analytical and simulation results, with a maximum error of only 2%. This is due to the data dependency of the final formula in Theorems, which allows for a comparison of the two curves on average.

1) *Short-Range Target*: To examine the finer details of the short-range in Fig. 6, we created a new plot that focuses solely on the short-range curves, as shown in Fig. 7. The performance of ZP-sequences with coherent integration at 20 dB SNR is demonstrated in this figure. Nevertheless, the outcomes reveal that the number of samples acquired in the GI is inadequate to attain a satisfactory detection performance in short-range situations such as 75 m when compared to medium and long-range scenarios. This was elaborated further in the discussion of Fig. 2. Given the short-range circumstances, it is clear that performance needs to be enhanced to achieve satisfactory target detection. One approach is to establish a high threshold for obtaining a high-quality waveform, as outlined in Section II-C. Generating a transmit waveform using random data streams from communications often necessitates multiple transmissions to locate a signal that satisfies the higher thresholds, resulting in a time delay that could span up to several CPs.

2) *Long-Range Target*: Fig. 8 compares the performance of ZP-SC-FDMA and ZP-OFDM in coherent processing at a long

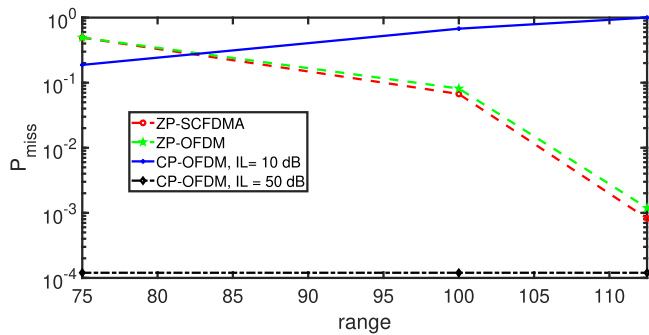


Fig. 9. The trade-off shows in which range [m], it is useful to switch to zero-padded OFDM/ SC-FDMA.

range of 112.5 m. The figure illustrates that ZP-SC-FDMA continues to outperform ZP-OFDM even at long ranges, although the difference is not as substantial as observed at medium ranges (as depicted in Fig. 6). Specifically, when p_{fa} is kept constant at 10^{-3} , the difference in p_d between the two waveforms is only 0.0005. The reason behind this is that both waveforms have sufficient power for detection at longer ranges since the echoes last for a longer time, as discussed in Fig. 2 and its subsequent discussion. In addition, a minor discrepancy of 0.1% can be observed in Fig. 8 between simulation and analytical results due to the use of an average of transmit data to plot the result of Theorem 5.

B. Trade-off Between the Performance of ZP-Sequences and CP-OFDM

We analyzed the performance of different ranges in detecting targets for various waveforms, as depicted in Fig. 9. The plot was generated for the miss-detection probability, $p_{miss} = 1 - p_d$, as a function of different target ranges. We maintained a constant received SNR of 20 dB, implying higher transmit power for longer ranges than shorter ones. At 112.5 m target range, the blue curve with an isolation level of 10 dB suffered due to low isolation for SI, and high power was required for this long range to achieve the SNR of 20 dB, generating stronger SI compared to short-range. However, for shorter ranges at 75 m, CP-OFDM outperformed ZP-sequences.

Additionally, Fig. 9 demonstrates that ZP-sequences exhibit superior performance to CP-OFDM when the isolation is low and the range is medium to long. Moreover, the figure displays that CP-OFDM performs well at 50 dB isolation when the target is within the unambiguous range region of the transmitter, regardless of the proximity of the range bin (black curve).

By comparing ZP-sequences to CP-OFDM with low isolation (10 dB) at longer ranges, we observe that the former has a lower value of p_{miss} . This is because the primary limitation for CP-OFDM is the SI, while ZP-sequences are not impacted by it. However, for CP-OFDM with high isolation (50 dB), p_{miss} is at its lowest point of approximately 10^{-4} . This demonstrates that achieving high TX-RX isolation leads to minimal SI, which in turn enhances the p_{miss} . Furthermore, a trade-off point in range between CP-OFDM with various isolation levels and the proposed ZP-sequences is obvious in Fig. 9. It implies that at a specific level of isolation, there is a range value beyond which utilizing ZP-sequences rather than CP-OFDM is suggested.

For instance, in this case, using ZP-sequences above 83 m is preferable to using CP-OFDM with a low level of isolation.

From Fig. 9, it can be observed that ZP-SC-FDMA outperforms ZP-OFDM marginally across all ranges, which can be attributed to the higher PAPR of the latter (refer to Remark 1). The maximum difference in performance is observed in the medium range, i.e., 100 m. At low ranges around 75 m, the performances are comparable as there are insufficient samples available for both cases. For higher ranges like 112.5 m, ZP-SC-FDMA is still the preferred choice over ZP-OFDM as it exhibits a lower p_{miss} and approximately 0.2% (see Fig. 8) improvement in target detection.

It is important to note that utilizing the idle interval in ZP-sequences for radar detection is advantageous due to its lower complexity. This method only requires a single RF chain and enables easy switching between transmit and receive modes in time-division duplexing (TDD) systems. In contrast, CP-OFDM always requires FD with high isolation, making it less efficient in this regard.

VI. CONCLUSION

Though full-duplex transceivers with properly tailored analog and digital SI cancellation for TX-RX SI suppression of CP-OFDM radars have been developed in the literature, they are power hungry and costly solutions. We proposed a novel method to eliminate the SI using zero-padded (ZP) orthogonal frequency-division multiplexing (OFDM) and single-carrier frequency-division multiple access (SC-FDMA), instead of the more widespread cyclic-prefix (CP)-OFDM. ZP-sequences do not need full-duplex for the monostatic radar operation, as there is no SI between the transmit and receive antennas during the guard interval (GI), which can be used for radar detection. This advantage depends on the target range, since this will determine the amount of gathered energy in the GI.

Furthermore, We derived the required radar receiver processing for ZP-sequences and CP-OFDM in time and frequency domains, respectively, to show that when the SI is high, ZP-sequences can be beneficial. Moreover, we proved analytically that the low peak-to-average power ratio (PAPR) of ZP-SC-FDMA, when compared to ZP-OFDM, is beneficial in time-domain radar processing. This is demonstrated also by means of numerical simulation with ROC curves, for all the candidate waveforms in both coherent and incoherent receiver processing.

It is worth noting that the option to make the GIs variable is a potential avenue for increasing flexibility in the system that requires efficient utilization of temporal resources based on the need of communications and radar. However, this aspect remains a topic for future exploration.

APPENDIX A

The binary hypothesis of Lemma 6, can be reformulated as following:

$$\hat{h}_i \sim \begin{cases} \mathcal{CN}(Mh_i, \sigma_h^2(i)), & \text{under } \mathcal{H}_1 \\ \mathcal{CN}(0, \sigma_h^2(i)), & \text{under } \mathcal{H}_0. \end{cases}$$

The likelihood ratio test (LRT) is given by

$$\mathcal{L}(\hat{h}_i) = \frac{p(\hat{h}_i|\mathcal{H}_1)}{p(\hat{h}_i|\mathcal{H}_0)}, \quad (120)$$

Let $\sigma^2 := \sigma_h^2(i)$, $\eta_i := Mh_i/\sigma_h(i)$, we have

$$p(\hat{h}_i|\mathcal{H}_1) = \frac{1}{\pi\sigma^2} \exp\left(-\frac{1}{\sigma^2}(\hat{h}_i - \eta_i)^*(\hat{h}_i - \eta_i)\right) \quad (121)$$

and

$$p(\hat{h}_i|\mathcal{H}_0) = \frac{1}{\pi\sigma^2} \exp\left(-\frac{1}{\sigma^2}|\hat{h}_i|^2\right). \quad (122)$$

The LRT is simplified as follows

$$\begin{aligned} \mathcal{L}(\hat{h}_i) &= \exp\left(-\frac{1}{\sigma^2}(\hat{h}_i - \eta_i)^*(\hat{h}_i - \eta_i) + |\hat{h}_i|^2\right) \\ &= \exp\left(\frac{1}{\sigma^2}\left(-|\hat{h}_i|^2 + \eta_i^*\hat{h}_i + \hat{h}_i^*\eta_i - |\eta_i|^2 + |\hat{h}_i|^2\right)\right), \end{aligned} \quad (123)$$

$$\begin{aligned} \sigma^2 \ln(\mathcal{L}(\hat{h}_i)) &= \eta_i^*\hat{h}_i + \hat{h}_i^*\eta_i - |\eta_i|^2 \\ &= 2 \operatorname{Re}\left\{\frac{Mh_i\hat{h}_i^*}{\sigma_h^2(i)}\right\} - |\eta_i|^2. \end{aligned} \quad (124)$$

Now, the decision variable is dependent on an unknown variable h_i that its maximum likelihood (ML) estimation is given by $h_i = \hat{h}_i/M$. We plug this into the LRT to get the generalized LRT

$$\sigma^2 \ln(\mathcal{L}(\hat{h}_i)) = 2 \operatorname{Re}\left\{\frac{|\hat{h}_i|^2}{\sigma_h^2(i)}\right\} - |\eta_i|^2 = \frac{|\hat{h}_i|^2}{\sigma_h^2(i)}, \quad (125)$$

which implies that $\frac{|\hat{h}_i|^2}{\sigma_h^2(i)}$ is the sufficient statistic.

REFERENCES

- [1] C. de Lima et al., "Convergent communication, sensing and localization in 6G systems: An overview of technologies, opportunities and challenges," *IEEE Access*, vol. 9, pp. 26902–26925, 2021.
- [2] S. H. Dokhanchi, B. Shankar Mysore, K. V. Mishra, and B. Ottersten, "Enhanced automotive target detection through radar and communications sensor fusion," in *Proc. IEEE Int. Conf. Acoust., Speech, Signal Process.*, 2021 pp. 8403–8407.
- [3] C. Aydogdu, M. F. Keskin, N. Garcia, H. Wymeersch, and D. W. Bliss, "RadChat: Spectrum sharing for automotive radar interference mitigation," *IEEE Trans. Intell. Transp. Syst.*, vol. 22, no. 1, pp. 416–429, Jan. 2021.
- [4] N. González-Prelcic, R. Méndez-Rial, and R. W. Heath Jr., "Radar aided beam alignment in mmWave V2I communications supporting antenna diversity," in *Proc. IEEE Inf. Theory Appl. Workshop*, 2016, pp. 1–7.
- [5] F. Liu, L. Zhou, C. Masouros, A. Li, W. Luo, and A. Petropulu, "Toward dual-functional radar-communication systems: Optimal waveform design," *IEEE Trans. Signal Process.*, vol. 66, no. 16, pp. 4264–4279, Aug. 2018.
- [6] X. Liu, T. Huang, N. Shlezinger, Y. Liu, J. Zhou, and Y. C. Eldar, "Joint transmit beamforming for multiuser MIMO communications and MIMO radar," *IEEE Trans. Signal Process.*, vol. 68, pp. 3929–3944, 2020.
- [7] F. Liu, Y.-F. Liu, A. Li, C. Masouros, and Y. C. Eldar, "Cramer-Rao bound optimization for joint radar-communication beamforming," *IEEE Trans. Signal Process.*, vol. 70, pp. 240–253, 2022.
- [8] B. Paul, A. R. Chiriyath, and D. W. Bliss, "Survey of RF communications and sensing convergence research," *IEEE Access*, vol. 5, pp. 252–270, 2016.
- [9] S. H. Dokhanchi, B. S. Mysore, K. V. Mishra, and B. Ottersten, "A mmWave automotive joint radar-communications system," *IEEE Trans. Aerosp. Electron. Syst.*, vol. 55, no. 3, pp. 1241–1260, Jun. 2019.
- [10] S. H. Dokhanchi, M. R. B. Shankar, M. Alaae-Kerahoodi, and B. Ottersten, "Adaptive waveform design for automotive joint radar-communication systems," *IEEE Trans. Veh. Technol.*, vol. 70, no. 5, pp. 4273–4290, May 2021.
- [11] P. Kumari, J. Choi, N. González-Prelcic, and R. W. Heath, "IEEE 802.11ad-based radar: An approach to joint vehicular communication-radar system," *IEEE Trans. Veh. Technol.*, vol. 67, no. 4, pp. 3012–3027, Apr. 2018.
- [12] P. Kumari, S. A. Vorobyov, and R. W. Heath, "Adaptive virtual waveform design for millimeter-wave joint communication-radar," *IEEE Trans. Signal Process.*, vol. 68, pp. 715–730, 2020.
- [13] S. Dwivedi, A. N. Barreto, P. Sen, and G. Fettweis, "Target detection in joint frequency modulated continuous wave (FMCW) radar-communication system," in *Proc. 16th Int. Symp. Wireless Commun. Syst.*, 2019, pp. 277–282.
- [14] C. B. Barneto et al., "Full-duplex OFDM radar with LTE and 5G-NR waveforms: Challenges, solutions, and measurements," *IEEE Trans. Micro. Theory Techn.*, vol. 67, no. 10, pp. 4042–4054, Oct. 2019.
- [15] C. Sturm and W. Wiesbeck, "Waveform design and signal processing aspects for fusion of wireless communications and radar sensing," *Proc. IEEE*, vol. 99, no. 7, pp. 1236–1259, Jul. 2011.
- [16] S. H. Dokhanchi, M. R. B. Shankar, T. Stifter, and B. Ottersten, "OFDM-based automotive joint radar-communication system," in *Proc. IEEE Radar Conf.*, 2018, pp. 0902–0907.
- [17] M. F. Keskin, H. Wymeersch, and V. Koivunen, "MIMO-OFDM joint radar-communications: Is ICI friend or foe?," *IEEE J. Sel. Topics Signal Process.*, vol. 15, no. 6, pp. 1393–1408, Nov. 2021.
- [18] L. de Oliveira, M. Alabd, B. Nuss, and T. Zwick, "An OCDM radar-communication system," in *Proc. Eur. Conf. Antennas Propag.*, 2020, pp. 1–5.
- [19] L. Gaudio, M. Kobayashi, G. Caire, and G. Colavolpe, "On the effectiveness of OTFS for joint radar parameter estimation and communication," *IEEE Trans. Wireless Commun.*, vol. 19, no. 9, pp. 5951–5965, Sep. 2020.
- [20] V. Singh, A. Gadre, and S. Kumar, "Full duplex radios: Are we there yet?," in *Proc. 19th ACM Workshop Hot Topics Netw.*, 2020, pp. 117–124.
- [21] Y. Zeng, Y. Ma, and S. Sun, "Joint radar-communication: Low complexity algorithm and self-interference cancellation," in *Proc. IEEE Glob. Commun. Conf.*, 2018, pp. 1–7.
- [22] A. Tang, S. Li, and X. Wang, "Self-interference-resistant IEEE 802.11 ad-based joint communication and automotive radar design," *IEEE J. Sel. Topics Signal Process.*, vol. 15, no. 6, pp. 1484–1499, Nov. 2021.
- [23] C. B. Barneto, T. Riihonen, S. D. Liyanaarachchi, M. Heino, N. González-Prelcic, and M. Valkama, "Beamformer design and optimization for full-duplex joint communication and sensing at mmWaves," *IEEE Trans. Commun.*, vol. 70, no. 12, pp. 8298–8312, Dec. 2022, doi: [10.1109/TCOMM.2022.3218623](https://doi.org/10.1109/TCOMM.2022.3218623).
- [24] C. Morgenstern et al., "Analog self-interference mitigation for IBFD, joint radar-communications in vehicular applications," in *Proc. IEEE Radar Conf.*, 2022, pp. 1–6.
- [25] R. J. Fitzgerald, "Effects of range-doppler coupling on chirp radar tracking accuracy," *IEEE Trans. Aerosp. Electron. Syst.*, vol. AES-10, no. 4, pp. 528–532, Jul. 1974.
- [26] T. Oyedare, V. K. Shah, D. J. Jakubisin, and J. H. Reed, "Interference suppression using deep learning: Current approaches and open challenges," *IEEE Access*, vol. 10, pp. 66238–66266, 2022.
- [27] B. Muquet, Z. Wang, G. Giannakis, M. de Courville, and P. Duhamel, "Cyclic prefixing or zero padding for wireless multicarrier transmissions," *IEEE Trans. Commun.*, vol. 50, no. 12, pp. 2136–2148, Dec. 2002.
- [28] S. H. Dokhanchi, A. N. Barreto, and G. Fettweis, "A half-duplex joint communications and sensing system using ZP-OFDM," in *Proc. IEEE 2nd Int. Symp. Joint Commun. Sens.*, 2022, pp. 1–6.
- [29] M. Shankar and K. Hari, "Reduced complexity equalization schemes for zero padded OFDM systems," *IEEE Signal Process. Lett.*, vol. 11, no. 9, pp. 752–755, Sep. 2004.
- [30] S. D. Blunt, J. G. Metcalf, C. R. Biggs, and E. Perrins, "Performance characteristics and metrics for intra-pulse radar-embedded communication," *IEEE J. Sel. Areas Commun.*, vol. 29, no. 10, pp. 2057–2066, Dec. 2011.
- [31] M. A. Richards, *Fundamentals of Radar Signal Processing*. New York, NY, USA: McGraw-Hill, 2014.
- [32] A. Ojha, "Characteristics of complementary coded radar waveforms in noise and target fluctuation," in *Proc. Southeastcon*, Charlotte, NC, USA, 1993, p. 4, doi: [10.1109/SECON.1993.465754](https://doi.org/10.1109/SECON.1993.465754).
- [33] J. Jorgensen, "Digital demodulator for wide bandwidth SAR," in *Proc. IEEE Int. Geosci. Remote Sens. Symp. Taking Pulse Planet: Role Remote Sens. Manag. Environ.*, 2000, vol. 5, pp. 2269–2271.
- [34] C. H. Jung and Y. K. Kwag, "PSLR estimation considering clutter background from SAR image data," in *Proc. IEEE Int. Geosci. Remote Sens. Symp.*, 2009, vol. 4, pp. IV-597–IV-600.
- [35] H. G. Myung, J. Lim, and D. J. Goodman, "Single carrier FDMA for uplink wireless transmission," *IEEE Veh. Technol. Mag.*, vol. 1, no. 3, pp. 30–38, Sep. 2006.
- [36] H. G. Myung, "Introduction to single carrier FDMA," in *Proc. 15th Eur. Signal Process. Conf.*, 2007, pp. 2144–2148.
- [37] S. Boyd and L. Vandenberghe, *Convex Optimization*. Cambridge, U.K.: Cambridge Univ. Press, 2004.
- [38] S. M. Kay, *Fundamentals of Statistical Signal Processing*, vol. 10. Englewood Cliffs, NJ, USA: Prentice-Hall, 1993, Art. no. 151045.
- [39] E. Dahlman, S. Parkvall, and J. Skold, *5G NR: The Next Generation Wireless Access Technology*. New York, NY, USA: Academic, 2020.



Sayed Hossein Dokhanchi received the B.S. degree in electrical engineering from the Sharif University of Technology, Tehran, Iran, in 2007, and the M.S. degree in electrical engineering from the Iran University of Science and Technology, Tehran, in 2010, and the Ph.D. degree in electrical engineering from the University of Luxembourg, Esch-sur-Alzette, Luxembourg, in 2020. From 2010 to 2016, he was with Telecommunications Infrastructure Company, Tehran, Iran. He is currently a Researcher with the Barkhausen-Institut, Dresden, Germany, under the guidance of Professor Fettweis. He has authored numerous papers for IEEE conferences and journals. His research focuses on signal processing for 6G networks.



André Noll Barreto (Senior Member, IEEE) received the M.Sc. degree in electrical engineering from Catholic University, Rio de Janeiro, Brazil, in 1996, and the Ph.D. degree in electrical engineering from Technische Universität Dresden, Dresden, Germany, in 2001. He has held several positions with academia and industry in Switzerland (IBM Research) and Brazil (Claro, Nokia Technology Institute/INDT, Universidade de Brasília, and Ektrum). He was the Chair with the Centro-Norte Brasil Section of the IEEE, in 2013 and 2014, and the General Co-Chair of the Brazilian Telecommunications Symposium, in 2012. From 2018 to 2022, he was with the Barkhausen Institut, Dresden, Germany. Since September 2022, he has been a Researcher with Nokia, Paris. His research interests include joint communications and sensing and physical-layer security for 6G.



Gerhard P. Fettweis (Fellow, IEEE) received the Ph.D. degree under H. Meyr from RWTH Aachen, Aachen, Germany, in 1990. After a Postdoc with IBM Research, San Jose, CA, USA, he joined TCSI, Berkeley, CA, USA. Since 1994, he has been a Vodafone Chair Professor with TU Dresden, Dresden, Germany. Since 2018, he is also the founding Director/CEO with the Barkhausen Institute, Dresden, Germany. His team spun-out 18 tech, and three non-tech startups. He initiated four platform companies. His research interests include wireless transmission and chip design, coordinates 5G++ Lab Germany. He is the Member of the German Academy of Sciences (Leopoldina), and German Academy of Engineering (acatech), and active in helping organize IEEE conferences.